A COMPUTATIONAL FLUID DYNAMICS (CFD) ANALYSIS OF THE AERODYNAMIC EFFECTS OF

THE SEAMS ON A TWO-DIMENSIONAL REPRESENTATION OF A SOCCER BALL

A Thesis

presented to

the Faculty of California Polytechnic State University,

San Luis Obispo

In Partial Fulfillment

of the Requirements for the Degree

Master of Science in Aerospace Engineering

by

Allen Rohr

December 2018

COMMITTEE MEMBERSHIP

TITLE: A Computational Fluid Dynamics (CFD) Analysis of

the Aerodynamic Effects of the Seams on a Two-

Dimensional Representation of a Soccer Ball

AUTHOR: Allen Rohr

DATE SUBMITTED: December 2018

COMMITTEE CHAIR: David D Marshall, Ph.D.

Department Chair

Department of Aerospace Engineering

COMMITTEE MEMBER: Graham Doig, Ph.D.

Assistant Professor of Aerospace Engineering

COMMITTEE MEMBER: Aaron Drake, Ph.D.

Associate Professor of Aerospace Engineering

COMMITTEE MEMBER: Kim Shollenberger, Ph.D.

Professor of Mechanical Engineering

ABSTRACT

A Computational Fluid Dynamics (CFD) Analysis of the Aerodynamic Effects of the Seams on a Two-Dimensional Representation of a Soccer Ball

Allen R. Rohr

Most major sports today use a dedicated ball or projectile with specific shape, size, and surface geometry, except for soccer. Over the history of the sport, the surface geometry and design stayed relatively unchanged, sewn together using 32 pentagonal and hexagonal panels. However, recent innovations in panel designs differ substantially from the traditional 32 panel ball. The effects these new designs have on the aerodynamic characteristics of the ball have remained largely unknown, even with the influx of experimental research completed in the past decade. Experimental studies have been broad in scope, analyzing an entire ball in wind tunnels or full flow paths in trajectory analyses. Computational efforts have been too assumptive in flow conditions, such as a fully turbulent flow field, which has not yielded accurate representations of the flow phenomenon. This study investigates the aerodynamic effects of the seam on a two-dimensional representation of a non-rotating soccer ball using Computational Fluid Dynamics (CFD). By applying a transitional solver to the narrowed scope of a two-dimensional flow domain, with a single seam in cross-flow, the effects of the seam on the boundary layer and overall transient flow structure can be more accurately modeled. Data analysis suggests the seam produces a local effect on skin friction, however, that effect does not materialize into a premature boundary layer transition or delayed separation point, as predicted by literature. A detailed flow visualization is consistent with this result, displaying expected symmetric vortex shedding similar to a smooth cylinder, but not fully capturing the effects of the seam, reinforcing the need for expanding computational research efforts in this field.

ACKNOWLEDGMENTS

TABLE OF CONTENTS

LIST OF FIGURES

1   INTRODUCTION

1.1 Background on Sports, Soccer, and Impacts

1.1.1   Sports

Sports are one of the most influential global activities that reaches into all aspects of daily life. Whether it be a profession, recreation, fandom, or education, the field of sport is an integral part of human interaction. Economically, the sports industry has a projected worth between $480-620 billion and a faster growth rate than overall GDP rates [1]. With the stakes rising in competition and the reward for victory with it, a great deal of investment and expansion into sports engineering has followed in recent decades [26]. While the term may be new, sports engineering is an old science, dating back even to Sir Isaac Newton's analysis of the flight of a tennis ball. Due to vast technological advances in recent history, the application of engineering research in this field has had an increased effect on outcomes [26]. To ensure teams and athletes around the world can be the best, a great deal of work continues to be done to optimize equipment, apparel, accessories, and fields of play.

1.1.2   Soccer

Soccer (football, association football) has the largest stake in the global sports market. The FIFA World Cup™, a quadrennial global soccer tournament of nations like the Olympics, is one of the most watched events, with 3.2 billion total viewers for the 2014 event, and 1.013 billion for the final match [19]. This global impact makes soccer one of the most profitable sports. Global yearly revenues for soccer sports events are about $28 billion, which is almost as much as the combined revenues of all major US sports, Formula 1 racing, tennis, and golf [1]. Due to the high viewership and monetary pressures on the athletes, the international soccer governing body, Fédération Internationale de Football Association (FIFA®), aims to ensure fair and eventful matches. This extends to the standardization of equipment for the sport, which places controls on items such as the apparel of the athletes, the field of play, and most importantly, the soccer ball.

FIFA® has an issued testing protocol for which all soccer balls must pass to be acceptable for competitive play, known as the FIFA Quality Programme for Footballs. This testing manual is an extensive guide to the ways in which soccer balls are tested by licensed FIFA® testing professionals

which include circumference, max sphericity, rebound height, water absorption, weight, loss of pressure, shape/size retention, and material analysis [18]. However, there are no restrictions on ball design (other than circumference/sphericity) or surface geometry, which differs greatly with most other sports which have a single design for professional use, such as basketball or baseball. This lack of standardization has produced an influx of different soccer ball designs, which have evolved over time.
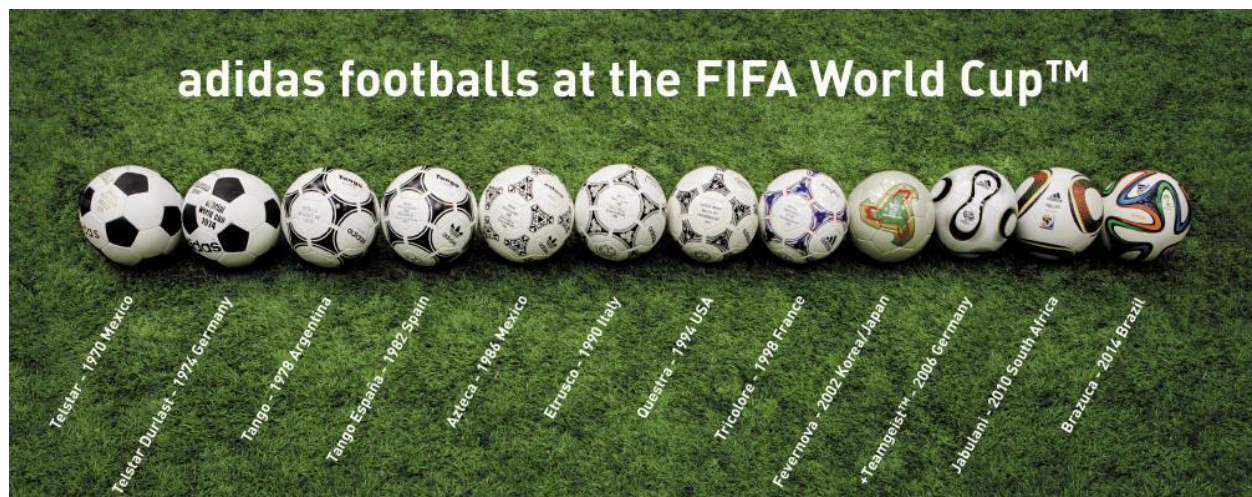
Figure 1: Evolution of the adidas Official World Cup Soccer Ball since 1970 [53]

In its introduction, soccer balls were made of leather with a rubber bladder, but recent technological advances in synthetic (waterproof) materials introduced a latex bladder with a polyurethane cover and a multi-layer, reinforced backing [39]. This synthetic material was used in the 1970 World Cup ball, which had 32 black and white hexagonal and pentagonal stitched panels, commonly referred to as the "traditional" soccer ball (This design was known as the "Buckyball" and was made with the black and white panels for players to better perceive swerve and curvature as well as better to see visually on the first televised broadcast of the World Cup in 1970). The design remained largely unchanged from the 32-panel design, until the 2006 World Cup ball, which featured a 14-panel design with various panel shapes including curved edges at the seams. In addition, the design evolved to thermally bonded panels, producing an overall smoother surface. The combination of technological advances in manufacturing methods along with the variation in surface design contributed to an overall change in the aerodynamic roughness of the surface of the ball [10]. The effects of the new surface designs are not considered in the

FIFA Quality Programme for Footballs Testing Manual, and therefore has created discrepancies in flight dynamics due to soccer balls with varying surface geometry.

1.2 State of Experimental Work

The increased investment and intrigue into sports engineering research has brought about a myriad of experimental work into the effects of soccer ball surface geometry on aerodynamic characteristics. This work includes wind tunnel testing, trajectory analysis, flow visualization, and computational analysis methods, to create a complete physical representation of the effects of these surface design changes. However, many of these studies have analyzed the geometry as a whole, rather than looking at specific cause-and-effect phenomenon of the seams and surface roughness on boundary layer transition, separation point, and wake structure [22].

1.2.1 Wind Tunnel Testing

Over the past decade, there have been extensive wind tunnel testing and flow visualization of various ball designs, surface geometry, and surface roughness [8-9,24-25,29-32]. The conclusions largely converged on the hypothesis that overall surface geometry of soccer balls alter the drag crisis to a lower Reynolds number in comparison to a smooth sphere, consistent with established work on surface roughening [4-5]. However, the asymmetry of the overall surface roughness due to the soccer ball panels creates differences in flight trajectory based off panel orientation, differing from the conventional symmetrically roughened sphere. [29] This analysis demonstrates that for non-spinning or low-spinning kicked balls the orientation has a large effect on flight trajectory, changing location of impact at the goal by up to 1 meter when comparing the 2010 and 2014 World Cup balls [29]. This change in final location as the ball crosses the goal line, for the exact same kick, would amount to the difference between scoring a goal, all simply due to the balls orientation at kick impact.

Other work has found similar results and considers effects related to spinning soccer balls [10,42]. The tendency of a spinning, translating ball to be deflected laterally is a result of the Magnus effect, a dominant flow characteristic for curled kicks [13]. This effect has an anomalous counter-action, the reverse Magnus effect, where the laterally induced motion would propagate in a direction opposite of the normal sense. This is a result of the ball transitioning through the drag crisis because of the change in velocity

during flight and the surface roughness' effect on the boundary layer on the advancing and retreating sides of the ball [13]. These effects are exacerbated by a smoother surface, much like a beach ball, and a subsequent roughening for the surface of a soccer ball is necessary for it to travel as expected in the case of spinning kicks. Experimental data illustrates that drag rises with increasing spin parameter and the Magnus force coefficient increases as well, which represents the induced side force [9].
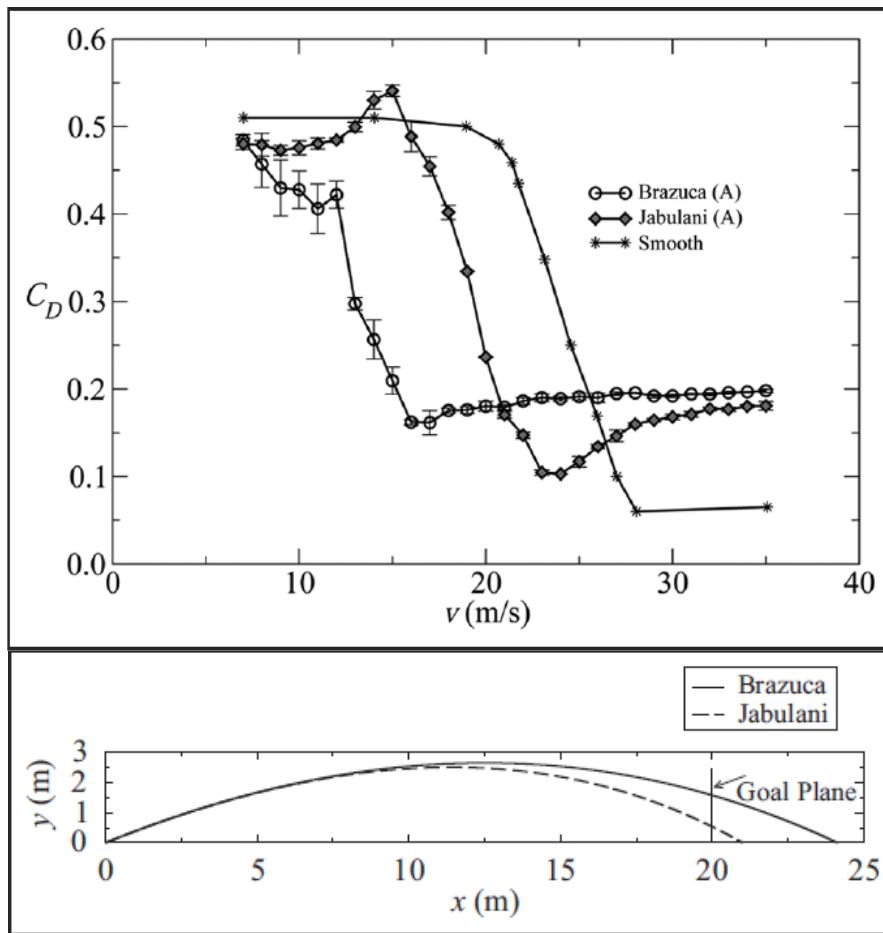
Figure 2: Top - Wind-Tunnel Experimental Drag Coefficient results for non-spinning Brazuca and Jabulani World Cup Balls. Bottom - Computational Trajectories for Brazuca and Jabulani balls kicked at 20 m/s at an angle of 22 degrees above the horizontal (Goff et. al 2014)

1.2.2   Trajectory Analyses

Trajectory analyses conducted alongside wind tunnel results and those done independently revealed differences in flight paths for differently designed balls, especially in the case of knuckling for non-spinning cases [16,23,39,52]. These studies reinforce the projections from wind tunnel testing and affirmed that the same ball with identical flow conditions hit with a different orientation produces a different trajectory [29]. Furthermore, the side forces produced by statistically smoother balls, such as the 2010 World Cup ball, were more likely to have larger knuckling tendencies at the speeds of normal free

Figure 3: Vortex Pathway for a non-rotating ball viewed from a wide angle (Asai et. al 2007)

kicks, due to the increased asymmetric forces in non-spinning kicks at these speeds [39]. Most importantly, "the magnitude of the lateral force is proportional to the square of the ball speed and so the knuckling effect will be exacerbated at the higher critical speed" [39], which happens to be the range of speeds in which typical soccer free kicks are taken.

1.2.3   Flow Visualizations

Flow visualizations have also been a crucial method for analyzing this complex flow phenomenon. Due to the inherent transient nature of this flow, flow visualization helps to create a well-rounded image of the overall flight of a ball, such as displaying wake structure due to roughness [39]. In addition, it can expose properties of the flow which can be missed through other means of analysis that make use of time-averaged values [9]. This approach has visually exposed the separation point effects, best seen in PIV analysis at the stream wise centerline of the ball [32]. The researchers followed the change in separation point due to different orientations of the ball fixed against the free-stream and

visualized the combined effect of different numbers and orientations of seams to the oncoming flow [32].

However, this method is inherently limited in the boundary layer region due to the minimum size of the

particles used in imagery techniques. To better visually model boundary layer effects computational

methods are required.

Figure 4: Velocity Vectors on the Suction Side of a non-spinning Soccer Ball in Four Different Kick
Orientations at Velocity 30 m/s [32]
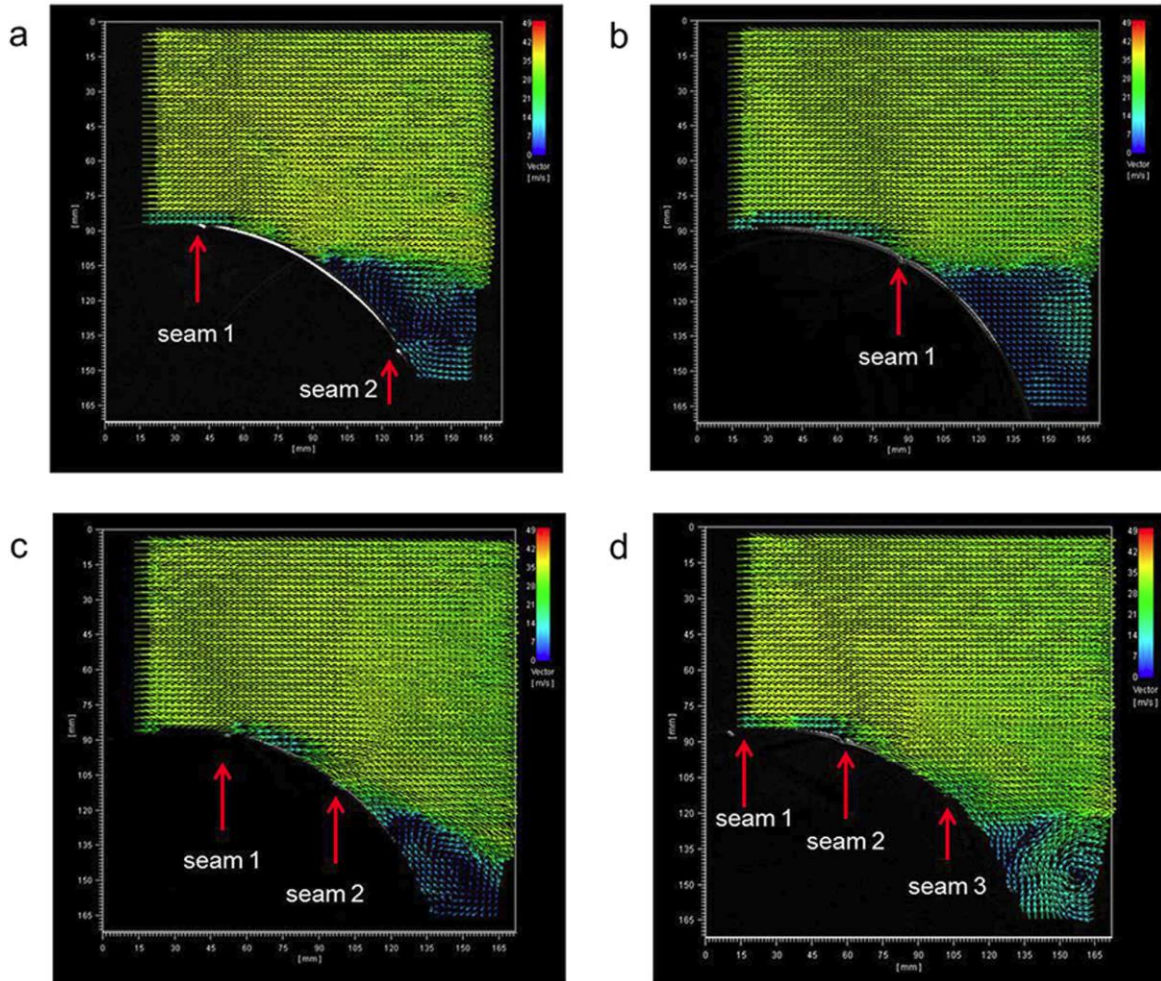
1.3 State of Computational Work

The computational analysis approach has become a dominant process in the engineering design and analysis of sports equipment [28]. The capability of computational analysis has improved over the past 30 years alongside modern CPU and RAM hardware advances [28]. However, sports ball analysis has only recently entered the field with relevance [28]. There is limited analysis of Computational Fluid Dynamics (CFD) work on sports balls due to the required computational power, difficulty of meshing, and a previous lack of demand for a highly detailed understanding [11]. Yet, the continued increase in computational power available and improved ability of commercially available software has led to the emergence of full ball CFD analyses [10-11,28]. These studies have developed the framework for CFD analyses in this field,
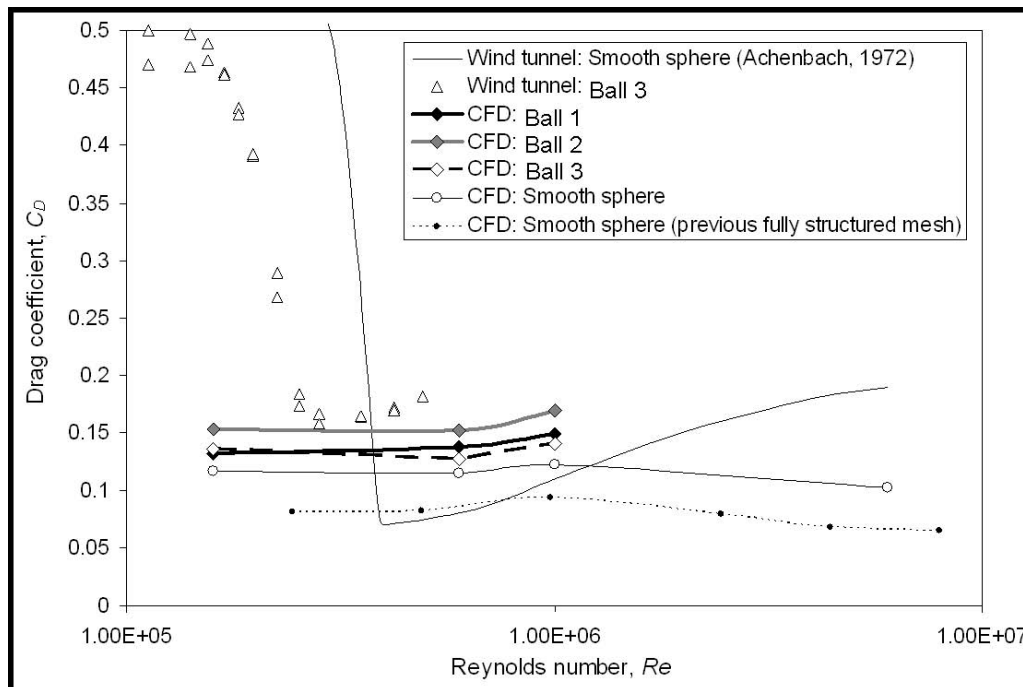
Figure 5: Drag Coefficient vs. Reynolds Number Comparison for Three Soccer Ball CFD Simulations to a Smooth Sphere [11]

but most assume fully turbulent flow domains which do not fully capture the flow characteristics [11].

1.4 Purpose of this Work

This study aims to fill a gap in the computational research by accurately modelling the effects of the seams on a soccer ball through Computational Fluid Dynamics (CFD). Using a turbulence model that accounts for boundary layer transition effects, a more complete computational solution can be derived. In addition, this study narrows the scope to a two-dimensional analysis of the effects of a single seam rather

7

than a full ball. The effect of a single seam on the boundary layer, separation point, and overall wake structure adds qualitative and quantitative support to experimental work. This study, in tandem with experimental work, creates a well-rounded analysis of the effects that seam design and geometry have on soccer ball aerodynamics.

2 METHODOLOGY

2.1 Theoretical Background

This study uses Computational Fluid Dynamics (CFD) which gives numerical approximation solutions to the governing equations of fluid flow. For this research, an applied approach was taken, using the commercially available software Ansys Fluent as the computational solver. Background on the way the governing equations are solved numerically are explained initially. Background on turbulence models and reasoning for the selection used for this study is described next. Finally, the overall framework for the solution process of this study is clarified in detail.

2.1.1 The Governing Equations

The Computational Fluid Dynamics process is based on the computational numerical solution of the governing equations of fluid dynamics. These result from the universal laws of conservation of mass, momentum and energy, resulting in the Continuity, Momentum, and Energy equations of fluid motion [44]. The derivations of these equations will not be presented here, but rather their form and manipulation for analysis using computational methods will be explored. Several key approximations are used to simplify the analysis of these equations:

1. A uniform, homogenous fluid without mass diffusion or finite-rate chemical reactions
2. Incompressible fluid
3. Thermal effects negligible
4. Newtonian fluid

From these approximations, the 3-dimensional governing equations for Continuity and Momentum take shape:

$$\text{Continuity: } \nabla * V = 0$$

$$\text{Momentum: } \rho \frac{DV}{Dt} = \rho f - \nabla p + \mu \nabla^2 V$$

Where ρ is the fluid density, V is the fluid velocity, f is the force per unit mass (body force), p is the pressure force, and μ is the coefficient of viscosity (considering constant) [44].

The components of the viscous momentum equation form the basis of the Navier-Stokes (NS) equations; however, the continuity and energy equations are included in the set [44]. For turbulent flow analysis, the unsteady NS equations are generally considered to govern the continuum regime [44]. This is where turbulence models come in as ways to numerically solve turbulent flow.

2.1.2   Turbulence Model Selection

Direct Numerical Simulation (DNS) is the most direct solution analysis for turbulent flow but requires all relevant time scales to be resolved from the smallest eddies to the order of the physical dimensions of the problem domain [44]. The time steps must be small enough to resolve small-scale motion in a time-accurate manner and the computation needs to be three-dimensional [44]. This creates an incredible demand on computer resources, not available for most applications today, including the present study.

Another approach is Large-Eddy Simulation (LES), in which the large-scale structure of the turbulent flow is computed directly and only the effects of the smallest (sub-grid scale) and more nearly isotropic eddies are modeled [44]. Using NS equation "filtering", a set of equations can be obtained that govern the "resolved" flow, based on a space averaging of the flow variables over regions approximately the size of the computational control volume (or cell) [44]. Much like DNS, LES solutions still demand large computational resources for complicated turbulent flows and for this reason was not used in the present study.

Most of the current modeling methods used in engineering applications of turbulent flow analysis are through the time-averaged NS equations, referred to as the Reynolds averaged Navier-Stokes (RANS) equations [44]. These equations are derived by decomposing the dependent variables in the conservation equations into time-averaged and fluctuating components, and then time averaging the entire equation [44]. The RANS equations for the Continuity and Momentum equations are written with bars over time averaged terms, shown in compressed form here:

$$\text{Continuity: } \frac{\partial \bar{u}_j}{\partial x_j} = 0$$

$$\text{Momentum: } \frac{\partial}{\partial t}(\rho \bar{u}_i) + \frac{\partial}{\partial x_j}(\rho \bar{u}_i \bar{u}_j) = -\frac{\partial \bar{p}}{\partial x_i} + \frac{\partial}{\partial x_j}(\bar{\tau}_{ij} - \rho \overline{u_i' u_j'}),$$

Where $\bar{\tau}_{ij}$ takes on the reduced form: $\bar{\tau}_{ij} = \mu\left(\frac{\partial \bar{u}_i}{\partial x_j} + \frac{\partial \bar{u}_j}{\partial x_i}\right), i, j, k = 1,2,3$

u_1, u_2, u_3 represent the three components of the velocity vector $\boldsymbol{V}$, x_1, x_2, x_3 represent the three components of the position vector, u' is the fluctuating velocity component, p is the pressure force, ρ is the fluid density, μ is the coefficient of viscosity (considering constant), and $\bar{\tau}_{ij}$ is the additional turbulent stresses [44]. Turbulence Models are required to represent the new terms, known as Reynolds Stresses, which are introduced to the NS equations, which involve mean values of products of rapidly varying quantities [56].

Turbulence models can be separated into two categories, those that make use of the Boussinesq assumption, or Eddy Viscosity Models (EVM), and those that don't, or Reynolds Stress Models (RSM) [44]. Boussinesq suggested that the apparent turbulent shearing stresses might be related to the rate of mean strain through an apparent scalar turbulent or "eddy" viscosity, and thus it was named after him [44].

For this study, a RANS approach was used due to the selection of a Turbulence model that is based off a two-equation EVM, the k-ω SST model. This model is derived from the original two-equation EVM which includes two transport equations to represent the turbulent properties of the flow. One of the transported variables is the turbulent kinetic energy, k, and the other is the specific dissipation, ω [56]. The Shear Stress Transport (SST) variation of the k- ω model accounts for the transport of the turbulence shear stress in the definition of the turbulent viscosity left out by other EVM models [7]. It does so by providing a limiter to the formulation of the eddy-viscosity and thus subsiding the over prediction resulting from not accounting for the transport of the turbulent shear stress [7]. The next section expands on the turbulence model selected for this study.

2.1.3   Transition SST Model

The main goal of this study is to precisely illustrate the boundary layer, transition, and separation, and therefore a turbulence model which can accurately represent this region was used. In Fluent, there are only three models of choice that offer transition prediction for wall boundary layers: The Transition SST model, the Intermittency model, and the Transition k-kl-ω [7]. The Transition SST model was selected over the other two models for the following reasons:

1. The Fluent user guide recommends the use of the Transition SST and Intermittency models over the k-kl-ω due to their combination with the SST model, which was designed to avoid freestream sensitivity of the k-ω model and is calibrated for accurate flow separation from smooth surfaces [7]

2. This study is not considering surfaces that move relative to the coordinate system (non-spinning body) and thus the Transition-SST model is sufficient because it is not Galilean invariant
   a. The Intermittency model is Galilean invariant, and thus suitable for surfaces that move relative to the coordinate system, therefore unnecessary for this study

3. The Transition SST model allows for user-defined empirical correlations and rough wall effects, which allows for expansion of the approach of this study to future work

The Transition SST model, based on the γ-Re_θ developed by Menter et. al., is also referred to as a Local Correlation-based Transition Model (LCTM) due to its combination of experimental correlations with locally formulated transport equations [40]. The solver couples the SST k-ω turbulence model with a transport equation for intermittency, γ, which is used to turn on the turbulent kinetic energy production term downstream of the transition point [40]. A second transport equation is solved in terms of the transition onset momentum-thickness Reynolds number ($Re_{\theta t}$) to capture the nonlocal influence of the turbulence intensity; an essential part of the model because it ties the empirical correlation to the onset criteria in the intermittency equation [40]. The title of this model, γ-Re_θ, is derived from the solution of these two transport equations [40].

2.2 CFD Framework

The following section serves as an architectural framework of the overall solution process used in this study. An auxiliary goal of this study is to create a basis of methodology for which further research can be expanded upon, both numerically and experimentally. First, the virtual geometry creation through computer aided design (CAD) is discussed. Next, the pre-processing procedure of flow domain meshing is explained. Finally, the computational solver and post-processing procedures are addressed.

2.2.1   CAD/Geometry Setup

2.2.1.1 Scope of Physical Domain Modeled

Due to the inherent complexity of the phenomenon under investigation, as stated in the previous section, the scope of the research was decided to be reduced as much as possible. Firstly, a full 3D model with resolution in the boundary layer necessary for the solver used to successfully capture transition effects would require more computational power than available in this study. Secondly, the goal of the study is to find specific effects of the seams, and for this goal, an examination of a single seam on an overall smooth body would give clarity to the specific effects it has on the aerodynamics. Thirdly, a limitation to a 2D physical domain would provide the necessary resolution to visualize the effects of the seam, much like 2D PIV in similar experimental works [32] and decrease computational resources necessary. For these reasons, experimental work which analyzed a cylinder with a single seam was used as comparison for the computational results, the setup of which is displayed in the figure below.
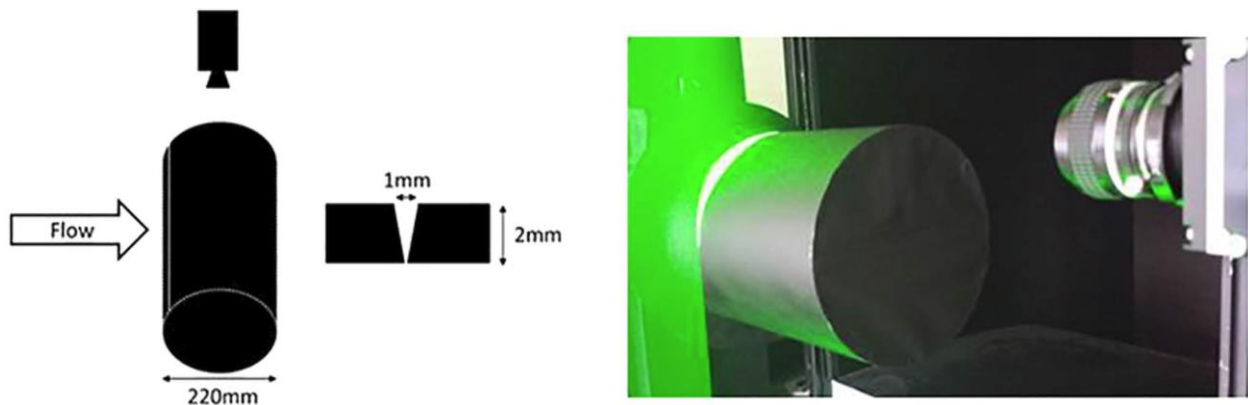
Figure 6: Experimental Set Up for Comparison in this Study (Hong et. al 2015)

The following Computer Aided Design (CAD) geometry was thus created based off the experimental work and concluded to be sufficient resolution for this study:

1. Two-Dimensional (2D) physical domain, resembling an "infinite" cylinder (see Figure 7)
2. Single seam, with height to width ratio h/b = 2, located at 75 and 65 degrees aft of "leading edge" or forward stagnation point (0 angle of incidence). Seam locations chosen for comparison to experimental results by Hong et. al 2015, which displayed largest effect of

single seam on flow over a circular cylinder at these locations (discussed in Chapter 3: Results)

3. Interface boundary (non-physical) at 1 ball diameter fore, up, and down from the surface of the body and through the wake for increased refinement in these areas

4. Overall domain 10 ball diameters in each direction, large enough far-field boundaries to see no effect on flow but not too large as to create wasted computational space
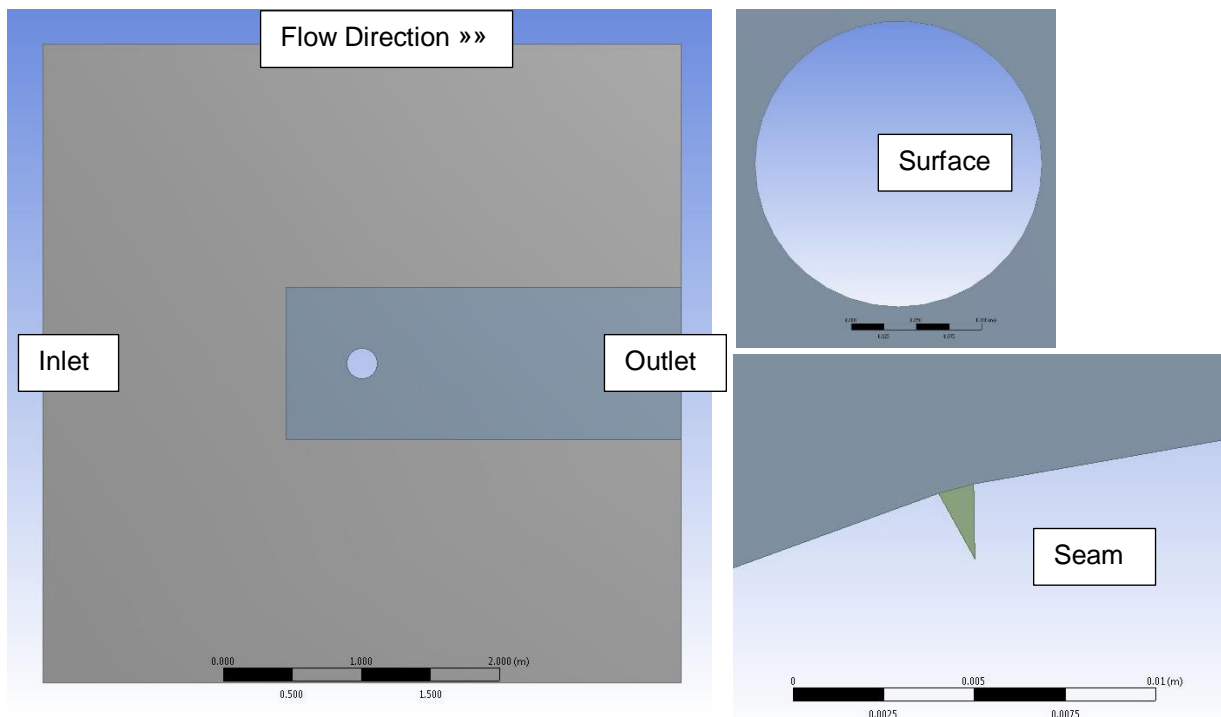
Figure 7: Computational Domain Used in this Study, for reference

2.2.1.2 Process of Physical Domain Creation

Several iterations were necessary until the CAD model was finalized. Initially, an "extruded" 2D cylinder was attempted, that brought the solution into a 3D physical domain. However, this method proved to be far too computationally intensive given the resources available. The far-field boundaries were finalized by initial guesses based off recommended distances from previous work [36,54] and the Fluent user's guide [7]. Then, validation cases of a smooth cylinder were solved until no induced effect from the boundaries could be seen. The interface boundary was found to be the most effective form of

14

localized refinement near the surface and in the wake regions aside from structured grid meshing, discussed in the next section.

The CAD modeling was initially undertaken through Solidworks, a separate software suite for CAD modeling from the Computational Solver. This approach was overtaken by using the built-in Ansys CAD modeling software due to preference in consistency between software interfaces for the entire solution process from geometry modeling to solution output. Thus, the Ansys Design Modeler was used for geometry and physical domain creation through the Ansys Workbench Project Management tool. Once the geometry was ready for computational domain meshing, checks for errors or holes in the geometry were conducted before continuing to the meshing phase.

2.2.2   Meshing

2.2.2.1 Meshing Background and Requirements

Once a complete geometric physical domain was completed, a computational mesh domain was generated using the Ansys Meshing tool. Several constraints for the meshing domain were imposed on the study due to the nature of the minuteness of the boundary layer in a physical sense. In addition, conditions outlined by the authors of the Transition-SST model and the software user manual guided the meshing of the region near the surface of the body. These constraints are as follows:

1. A wall-normal mesh resolution with $y^+<1$ and expansion factors smaller than 1.1 found to be the threshold for accuracy of the model in flat plate test cases to detect transition effects [7]
2. Fine mesh resolution in the location of transition necessary for separation-induced transition because it occurs over a short length [7]

There are two approaches to meshing the physical domain, structured and unstructured meshes (and a combination of both known as hybrid meshes). The former utilizes blocking, where the physical domain is divided into computational blocks in which the user can control node count, spacing, and growth ratios. The latter utilizes built-in meshing tools, either propriety or otherwise, which work to fill the physical domain with computational cells in several different ways. The method of choice in this application is discussed in the next section.

15

2.2.2.2 Meshing Process

Initially, a structured mesh was attempted for this study due to the ability to control boundary layer mesh cell growth and use an O-grid scheme near the surface. The O-grid scheme allows for mesh blocks that handle geometry curvature much better than standard hexagonal blocks. However, when using a structured approach with specified blocking edges in the mesh domain, computational solutions showed oscillations in computed wall fluxes such as wall shear stress.
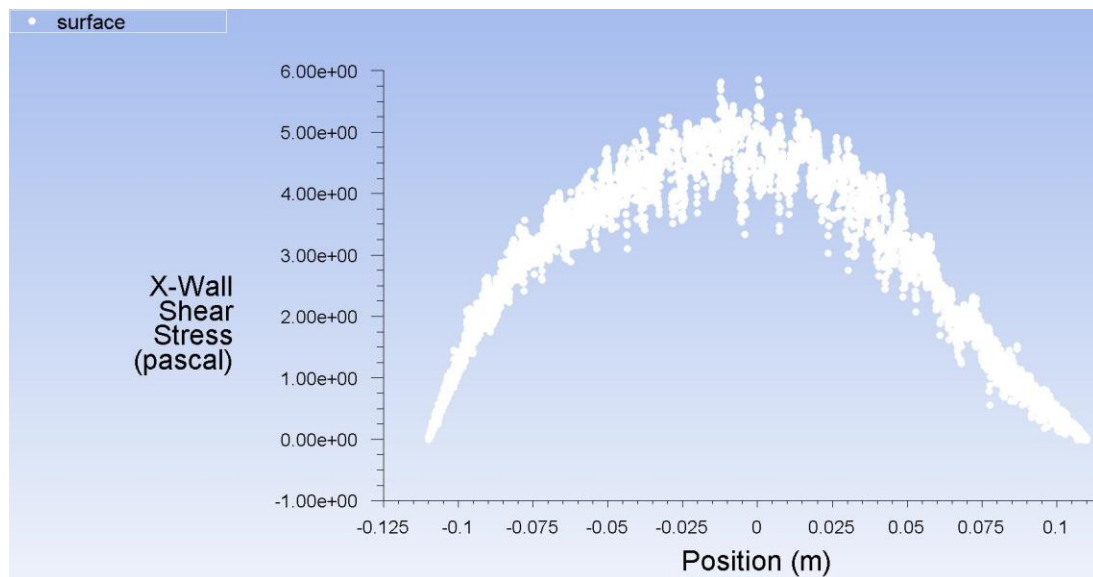
Figure 8: Oscillatory Wall Shear Stress Values Produced by Structured Mesh Blocking Method

In addition, an unstructured grid was more aligned with the auxiliary goal of this study, to create a framework for which further research may expand upon. Using an unstructured grid meshing tool allows researchers with less experience in the meshing process access to this type of flow analysis which they may otherwise have not attempted due to its complexity. Therefore, an unstructured mesh was used with several key properties which were necessary to capture the effects of this study computationally:

1. Inflation layer for boundary layer, which produces orthogonal cells which grow wall-normal to the surface boundary selected with explicit initial cell height, total cell number, and growth ratio

   a. To meet the requirements of the mesh resolution stated above, a 5% growth ratio was used with an initial wall spacing that kept $y^+<1$ for the Reynolds Number used in this study and a total 30 nodes in the boundary layer as recommended by the user's guide [7]

2. The unstructured meshing tool used was a hexa-dominant, patch independent, part meshing due to the robustness of this tool. Hexa-dominant is recommended over tri-based meshes due to the orthogonality of quad cells in comparison to tri cells [7]

3. Overall flow domain growth ratio limited to 1.1 (or 10 percent from cell to cell), to keep global aspect ratio low. Another recommended rule of thumb by the user's guide for high quality cells is a low aspect ratio, due to its benefit of lowering the probability of mesh-induced errors

4. The non-physical interface boundary mentioned in the CAD modeling was used as an interface between the near-field and far-field cells to be able to refine the cells near the surface of the body and in the wake region. The growth ratio from the interface boundary outward (from near-field to far-field cells) was low to ensure this interface boundary did not induce non-physical flow effects
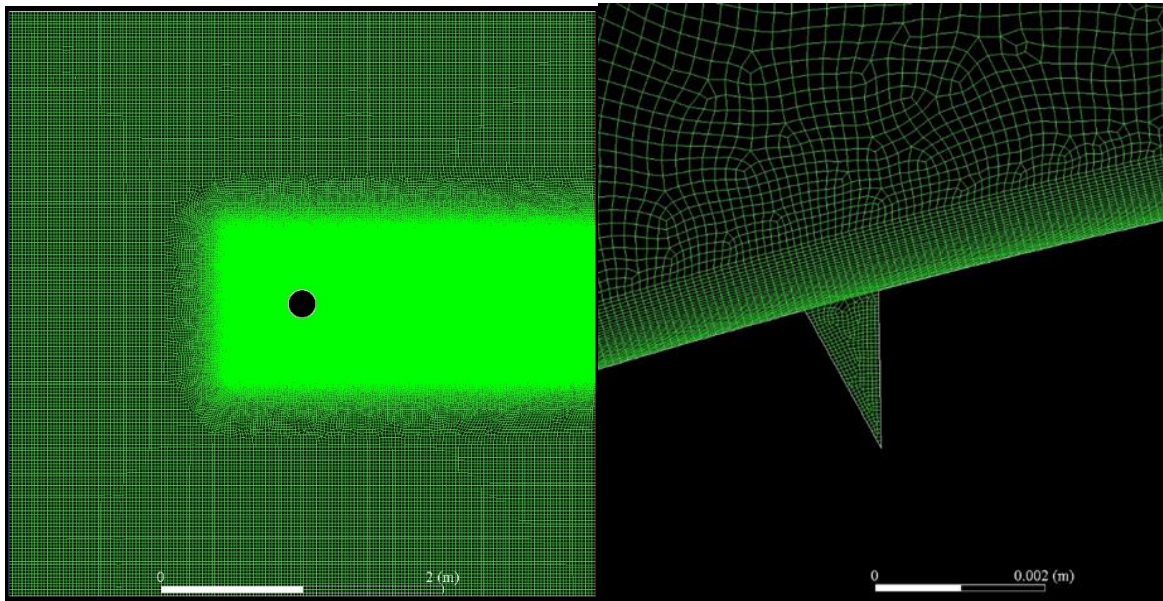
Figure 9: Computational Mesh Domain Including Detail of Mesh with Structured Boundary Layer Inflation Cells

2.2.2.3 Mesh Resolution

Once an initial computational meshing grid was created, it was exported for the Ansys Fluent solver for the smooth cylinder physical body. From there, the solution process was conducted and time-averaged values for Cd and Cl were used to validate the flow domain's accuracy. A Richardson Extrapolation – Grid Convergence Index (GCI) study was conducted for the meshes used in this work, detailed in the Results section.

The results discussed for comparison were conducted at the "medium" mesh resolution level for the smooth validation case and the seam case upon conclusion of the Grid Independence Study. Before exporting the mesh to the solver, built-in quality checks in the meshing tool are used to analyze the mesh for quality [7]. Some of the most important checks, according the Meshing User's Guide include the following [7]:

- Element Quality: the ratio of the volume to the sum of the square of the edge lengths for 2D quad/tri elements, or the square root of the cube of the sum of the square of the edge lengths for 3D elements. This ranges from 0 to 1, 1 indicating a perfect square or cube and 0 indicating zero or negative volume. An ideal element quality would be a value of 1

- Aspect Ratio: for quadrilaterals, the ratio of a longer side to a shorter side of a rectangular plane projected by rectangles through midpoints of each side of the cell, with the best possible aspect ratio being 1 (for a square). For triangles, a similar process is conducted however the rectangular plane projected by rectangles go through the midpoint of 3 sides and the triangle apex of the cell, with the best possible aspect ratio being 1 (for an equilateral).

- Cell Skewness: a ratio of how close to ideal (i.e., equilateral or equiangular) a face or cell is, with 0 being equilateral and 1 being degenerate. Degenerate cells are characterized by nodes that are nearly coplanar (collinear in 2D) and unacceptable due to the nature of the equations of the solver assuming relatively equilateral/equiangular cells. Ansys recommends values of 0.5 or smaller

The Ansys Meshing tool includes several built-in physics preferences depending on the analysis type for the user to use pre-assigned quality metrics to all the mesh quality criterion. For this reason, the CFD physics preference was used which applies more scrutiny on mesh and cell quality than all other physics preferences. The mesh was refined and edited to the recommendations of the errors and warnings found by the built-in mesh quality checker. The mesh was finally exported to Ansys Fluent for the initialization of the solution process once all mesh quality metrics met minimum quality metric recommendations.

2.2.3 Solver

After completing mesh quality checks and successfully exporting the mesh to the solver, the solution process was ready to be initialized. As stated previously, the computational solver used in this study was Ansys Fluent, and the use of Ansys Workbench provided a seamless transition of exporting the mesh from the meshing tool into Fluent for the initialization of the computational solution process. Several conditions were set in Fluent to ensure successful validation against the experimental cases used for comparison and reach convergence in the solution process. Several notable solution settings and properties are listed below:

- Flow domain settings:
  o 2D solution analysis (due to the 2D mesh domain)
  o Pressure-based solver, used over the density-based solver due to this solution process considering incompressible flow
  o Transient flow (time-variant) to capture vortex shedding and variation of separation point due to transient flow phenomenon
  o Physical properties for air defined as constant with density of 1.225 kg/m^3 and viscosity of 1.7894x10^{-5} kg/m-s.
  o Boundary Conditions as follows:
    ▪ Inlet Boundary: Velocity-Inlet with velocity of 24 m/s and normal to boundary, used for comparison to results by Hong et. al 2015 and relation to average soccer place kick velocity [35]. An Intermittency value of 1, 3% inlet turbulence intensity and turbulent length scale of 0.0154m, explained further in this section
    ▪ Outlet Boundary: Pressure-outlet, with gauge pressure of 0 Pascal and backflow calculated normal to boundary with identical turbulence properties to inlet condition
    ▪ Top and Bottom Far-Field Boundaries: Wall with slip condition (stationary wall with 0 wall shear stress) and roughness constant of 0 (smooth surface)

19

- Surface body: wall with no-slip boundary condition and roughness constant of 0 (smooth surface)

- Interface boundary: Interior condition as to be simply considered fluid domain cells and not impart non-physical effect on flow solution

- Transition SST-model related settings:

  o The Curvature Correction function was used due to its being recommended by the Fluent User's Guide when dealing with highly curved streamlines, such as flow over spherical or cylindrical bodies [7]

  o The Roughness Correlation was kept off for this solution due to the analysis of a smooth surface

  o No user defined transition correlations were used to assess the model predicted transition location

  o No Scale-Resolving Simulation options were added to the flow such as Detached Eddy Simulation (DES) due to the increase in necessary computational resources and divergence of solutions run with these options included

- Solver Settings:

  o The SIMPLE Pressure-Velocity Coupling method was used over the PISO method even though the Fluent User's Guide recommends the PISO algorithm for all transient flow calculations. This was due to the computational constraints of the PISO algorithm on small time steps, necessary for this solution to keep a low CFL number, explained further in this section

  o Second-Order Upwind Schemes were used for the spatial discretization schemes for increased accuracy due to the body curvature creating mesh cells not aligned directly with the freestream flow

  o A first-order implicit transient flow discretization scheme was used due to reduce computational resources necessary with respect to a second-order method

  o The default under-relaxation factors were used initially due to the recommendation from the Fluent User's Guide. An attempt to decrease computation time by increasing

20

the relaxation factors produced divergence issues in the solver and thus the default

relaxation factors were used for the model were used for the extent of the study

- A Time Step size of 4.5×10^{-5} seconds was used for the time discretization to keep the CFL (Courant-Freidrichs-Lewy) number low for accuracy in transient flows. The value was derived by the estimated period of vortex shedding from experimental values of Strouhal number at the corresponding Reynolds number for this study [6]

In addition to the specific settings above, an overall solution process included an initialization of the flow field with the laminar solver for 50 time steps. Then, the solver model was switched to the Transition-SST model with the conditions described previously for 10,000 time steps, which produced a converged solution with a minimum of 5 complete vortex shedding cycles determined by monitoring the Lift Coefficient time history value. This approach proved to converge the solution faster than without the laminar flow field initialization without effect to the converged solution values.

Several important surface and flow domain values were tabulated during the solution process to be able to generate accurate, time-averaged values for analysis. The pressure coefficient, skin friction coefficient, and x- and y- wall shear stresses were tabulated for each surface node at every time step over the entire solution process. This was done so that instantaneous values could be time-averaged over shedding cycles as well as compiled into time animations of solution variables. Overall flow domain data was saved every 10 time steps to create contour and vector animations for flow visualization at different instantaneous time steps. The data export was formulated to optimize data analysis using MatLab and Ansys' CFD-Post simulation results post-processor tool.

2.2.4 Post-Processing

The Post-Processing phase of the solution required data analysis using Ansys CFD-Post and MatLab. Due to the transient nature of the flow solution, instantaneous flow values were tabulated and exported for analysis in MatLab and overall flow solution data files were exported for analysis in CFD-Post. CFD-Post was chosen for the post-processing tool due to its seamless integration into the Ansys Workbench project management tool and export/import of data from Fluent to CFD-Post. MatLab was chosen for data analysis because of the author's proficiency in this programming language and the

program's ability to store and read large data files seen in this analysis. This section will provide detail on the specific post-processing techniques used in this study. The techniques used were selected to best represent the solution data for comparison to experimental values, as well as create easy to follow and visually informative illustrations of the flow phenomenon.

To create accurate time-averaged values for variables such as lift, drag, pressure, and skin friction coefficient, a vortex shedding cycle time-averaged (referred further as "cycle-averaged") value for these quantities had to be derived. The reason for this is the values oscillate depending on the temporal location of the vortex being shed from either the top or the bottom surface at any given time. With these cycle-averaged values, accurate comparisons to experimental data, which time-average aerodynamic force coefficients such as C_l and C_d, could be performed. For analysis of separation point, cycle-averaged values for c_f and C_p were tabulated and plotted for comparison with experimental data. Global time averaging of the solution data, or time-averaging the flow solution over the entire range of the solution time, was found to both cancel out and/or compound some of the data incorrectly. This data analysis was conducted using MatLab, taking advantage of the data store function for reading large database or file storage data files.

In CFD-Post, several modes of flow visualization were utilized including velocity vectors, path lines, and flood-fill contours of several flow properties. Velocity vectors were used to display the laminar separation bubble and turbulent reattachment region for boundary layer transition as well as the separated recirculation wake region. Flow particle path lines were used to create instantaneous visual representations of flow particle motion. Flood-fill contours were used to illustrate flow properties in the overall flow domain such as turbulence characteristics and visually inspect any mesh induced errors.

Time animations were used in the research process to visualize the transient values of flow properties for understanding and validation of flow physics. Time animations of surface related values such as c_f and C_p were generated in MatLab to investigate separation point and vortex shedding effects. Time animations of flow domain properties (using velocity vectors or flood-fill contours of other values) were generated in CFD-Post to visually support the c_f and C_p time animations.

2.2.5   <u>Grid Independence Study/Validation</u>

To validate the flow physics of the simulation, a grid independence study was conducted to ensure the mesh was refined enough to produce an accurate solution. Grid independence and quantification of uncertainty in CFD is an important aspect of numerical discretization, as every result is only accurate to a certain degree. However, concurrent methodology on an accurate discretization of numerical error is not well established. The author chose to follow the Journal of Fluids Engineering Editorial Policy guidelines which takes the approach of a more widely accepted CFD validation technique [47], built on the Richardson Extrapolation method.

The most well established and practiced method of discretization error estimation is the Richardson Extrapolation method, which has been referenced extensively by CFD studies over the years [47]. The Richardson Extrapolation, also known as the h^2 extrapolation, assumes the discrete solutions have a series representation, in the grid spacing h, of

$f = f[exact] + g_1h + g_2h^2 + g_3h^3 + \cdots$, where the functions $g_1, g_2, etc.$ are defined in the continuum and do not depend on any discretization [45]. This equation need only be a valid definition for the order of the discretization to be applied to finite element solutions [45]. For a second order method, $g_1 = 0$ above and the idea behind the Richardson Extrapolation becomes clear. Combining two separate discrete solutions, say f_1 and f_2, on two different grids with (uniform) discrete spacings of h_1(fine grid) and h_2 (coarse grid), to "eliminate the leading order error terms in the assumed error expansion" [45] and obtain a more accurate estimate of $f[exact]$ which takes the form of the original h^2 extrapolation by Richardson:

$$f[exact] = \frac{h_2^2 f_1 - h_1^2 f_2}{h_2^2 - h_1^2} + H.O.T.$$

where H.O.T are higher-order terms (Roache 1994). Using a grid refinement ratio $r = h_2/h_1$, where applying this, and dropping H.O.T., the previous equation takes the form:

$$f[exact] \approx f_1 + (f_1 - f_2)/(r^2 - 1)$$

and the most common application of this method is with a grid doubling or halving, or $r = 2$ (or ½) (Roache 1994). The Richardson Extrapolation is most often used with integer grid refinement, specifically

23

applied to grid doubling, however Roache points out that even in Richardson's 1910 paper that he looked forward to defining a continuum by higher-order interpolation [45].

From the Richardson Extrapolation, a fine-grid error estimator approximates the error in a fine-grid solution, f_1, by comparing it to that of the coarse grid, f_2, defined by

$$E_1^{fine} = \frac{\varepsilon}{1 - r^p}$$

and a coarse-grid error estimator approximates the error in a coarse-grid solution, f_2, by comparing the solution to that of a fine grid, f_1, defined by

$$E_1^{coarse} = \frac{r^p \varepsilon}{1 - r^p}$$

where $\varepsilon = f_2 - f_1$; f_2, f_1, and r are as mentioned above; and p = formal order of accuracy of the algorithm. To account for uncertainty in the generalized Richardson-based error estimates due to various factors and provide a basis for all grid-convergence studies as grid doubling with a second-order method, Roache [46] incorporates a safety factor, F_s, into the estimators and the Grid Convergence Index (GCI) is defined for the fine and coarse grid as

$$GCI_1^{fine} = F_s|E_1| \; ; \; GCI_2^{coarse} = F_s|E_2|$$

The safety factor is interpreted as the error band of the experimental data, with Fs<1, since Fs=1 gives GCI = |E|, or the best estimate of the error, analogous to a 50% error band [46]. Values for the safety factor were recommended by Roache through conservative estimates for any grid-convergence study to one with a grid doubling and a second-order method (r=2, p=2) [46]. From this methodology, Roache extracts convergence rate from grid-convergence tests and sources the calculation of the order, p, of the algorithm, for a constant r:

$$p = \frac{\ln\left(\frac{f_3 - f_2}{f_2 - f_1}\right)}{\ln(r)}$$

Where subscript 1 indicates the finest grid of three grid solutions. When r is not constant, the equation above cannot be used to calculate p because it is implicitly present in the GCIs, and a more general procedure is used to solve the equation for p:

$$\frac{\varepsilon_{23}}{r_{23}^{p} - 1} = r_{12}^{p}\left[\frac{\varepsilon_{12}}{r_{12}^{p} - 1}\right]$$

This equation is transcendental in p and requires iterative solution methodology to converge to the appropriate value for p according to the order of the solution [45]. To conduct this solution process and calculate the resulting GCI and associated error for grid solutions of this study, the procedure described in Journal of Fluids Engineering Editorial Policy guidelines [47] was followed for consistency to other works. It's step by step process has been posted as Appendix A.

3   RESULTS

Transient flow simulations were carried out on the smooth surface and 75-degree seam geometries at the same flow conditions and comparisons are drawn in the following sections. First, a comparison of pressure and skin friction distributions along the surface of both simulations and experimental data is explored. Next, a comparison of the aerodynamic force coefficients between both simulations and experimental data is examined. Finally, several different forms of flow visualizations are presented for qualitative discussion.

3.1 Pressure and Skin Friction Distribution Comparisons

The effects of the seam on the aerodynamic characteristics was presumed to be best represented by comparison of pressure and skin friction distribution with that of a smooth surface (representing a cylinder) and a geometry with a single seam. One limitation to this method is in the comparison of experimental data with that of computational data. Experimental data used for validation does not have clear methodology on the process of time-averaging transient data values, rather that the instrumentation used for force measurement handled that internally [2]. However, it is noted in other works that a time-averaged value is recorded over a set period to obtain a time-averaged solution [6,48]. Due to the occurrence of vortex shedding at the Reynolds number investigated in this study, a vortex shedding cycle averaged value was used for comparison to experimental results. This method was used to ensure the calculated value was not inadvertently averaged out by general time-averaging over the entire converged solution period.

3.1.1   Smooth Surface

Initially, a geometry with a smooth surface was simulated to ensure that the flow physics were correctly captured at the Reynolds Number investigated in this study. The smooth surface case was intended to validate the geometry by comparing the results to experimental data available at the same flow conditions. The following figures display the calculated coefficients of skin friction and pressure as they compare to established data on cylinders in cross-flow. The experimental data available was conducted for a sweep of Reynolds numbers, and so the two nearest values were displayed for comparison. The skin friction coefficient comparison shows good agreement with the experimental data in

capturing the boundary layer growth, separation bubble, turbulent reattachment, and subsequent

separation.
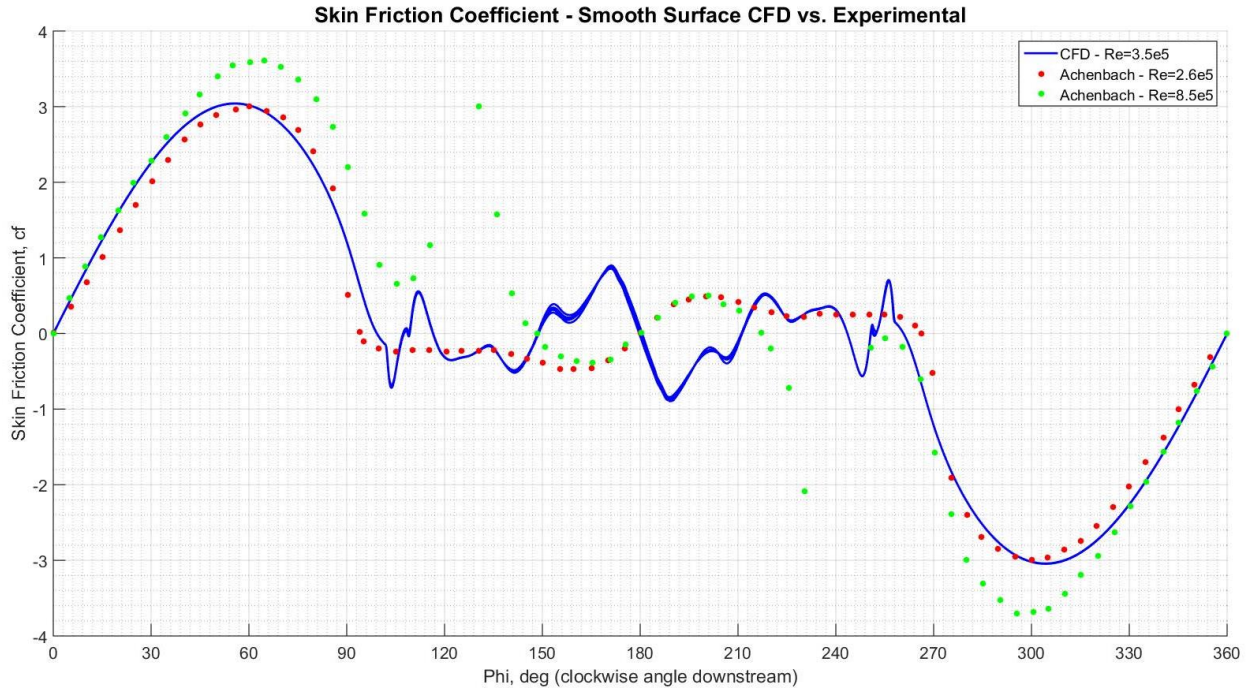
Figure 10: Skin Friction Coefficient Comparison of CFD to Experimental Data by Achenbach, 1968. (Skin Friction Coefficient was normalized for comparison to experimental data using the following: $cf = \frac{\tau_0}{\rho U_\infty} * \sqrt{Re}$)

However, it is noted that the CFD data displays more pronounced effects in the recirculation

region from the vortex shedding phenomenon, most clearly seen in the drop in pressure coefficient near

the 180° mark. This phenomenon was further investigated by looking at the range of instantaneous

values for skin friction and pressure coefficient over an entire vortex shedding cycle. In investigation of

these values, it was found that the vortex shedding cycle averaged values shown here aligned with the

instantaneous values over an entire vortex shedding cycle as well as over multiple shedding cycles, as is

aligned with experimental data acquisition methods.
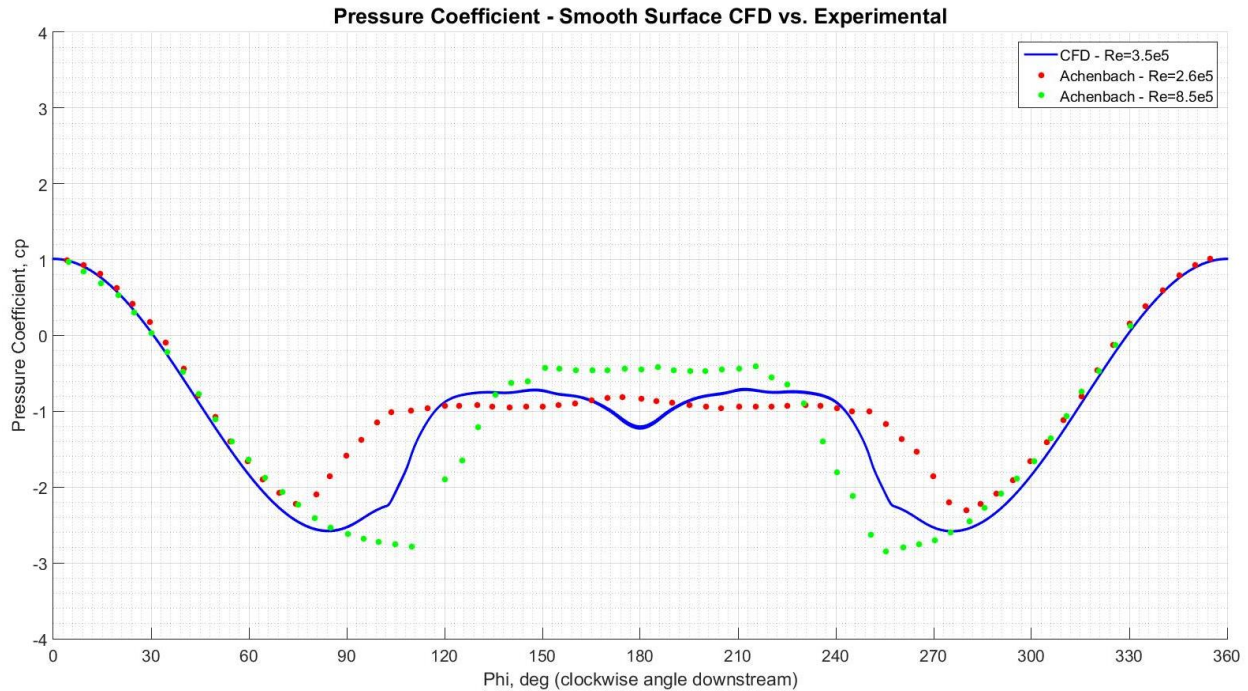
Figure 11: Pressure Coefficient Comparison of CFD to Experimental Data by Achenbach, 1968.

3.1.2   Single Seam at 75 degrees, h/b = 2

Once the flow physics were captured using a smooth case for validation, the geometry in question, relating to that seen in the validation experiment by Hong et. al 2015 [32] with a single seam on the top surface, was investigated. The seam was triangular, with a depth of 2mm and with of 1mm, giving a height to width ratio h/b = 2. The CFD data comparison with the smooth surface case shows that the seam is captured, as seen by the spike in skin friction coefficient, however, the effects as predicted by literature such as a delayed separation are not shown. After the spike in skin friction coefficient, the boundary layer profile quickly returns to the structure of the smooth surface case as seen in the figure below.

Figure 12: Skin Friction Coefficient Comparison - Single Seam at 75° (h/b=2) vs. Smooth Case CFD (Skin Friction Coefficient was normalized using the following: $cf = \frac{\tau_0}{\rho U_\infty} * \sqrt{Re}$)
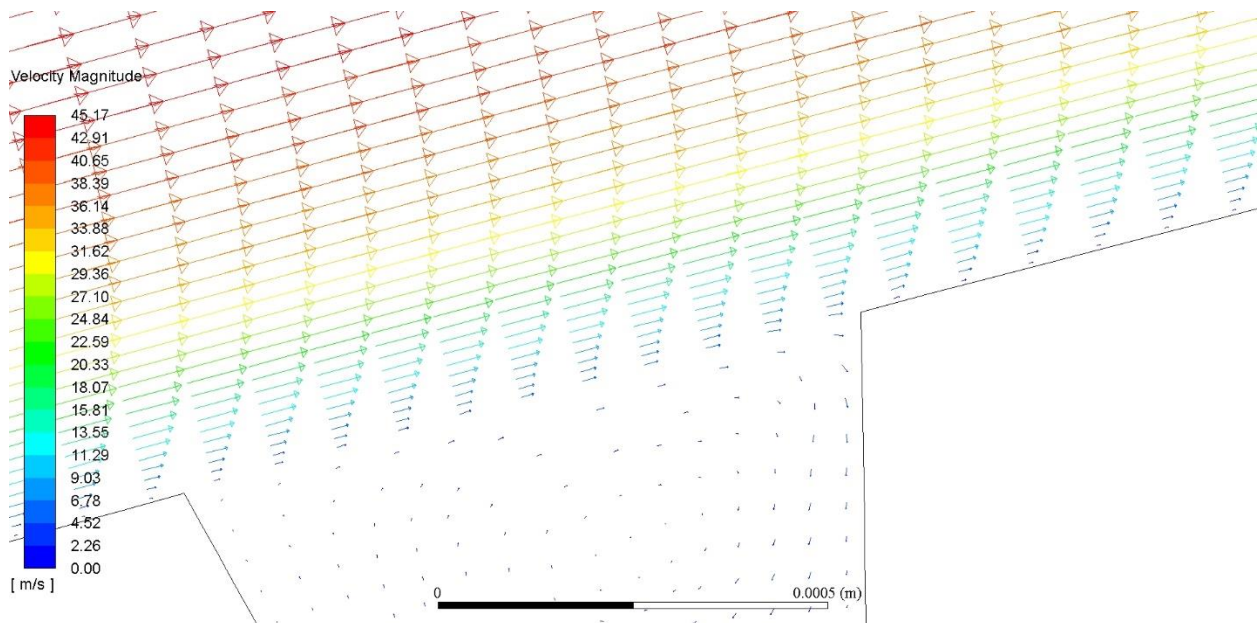
Figure 13: Velocity Vectors Colored by Magnitude for the Single Seam at 75° (h/b=2) CFD simulation

The pressure coefficient plot shows similar results, as there is a distinct drop in the pressure coefficient at the seam location, however there is no differentiation otherwise seen between the seam and the smooth case.

Figure 14: Pressure Coefficient Comparison - Single Seam at 75° (h/b=2) vs. Smooth Case CFD

3.1.3   Single Seam at 65 degrees, h/b = 2

The author investigated an additional location of the seam for comparison to the experimental work by Hong et. al 2015 [32] in order to have multiple data points for comparison to the experimental results. This was pursued due to the inconsistency with results from the single seam at 75 degree simulation with the experimental data, discussed previously. The 65° seam location was chosen due to the downward trend of the lift data between the tabulated values of 60° and 75° in the study[32]. It was hypothesized that a second solution value analyzed at the 65° seam location would provide thorough examination of the accuracy of the CFD methodology and ensure the initial solution was not an outlier. The skin friction and pressure distribution for this simulation are displayed below, with comparison to the smooth CFD simulation.
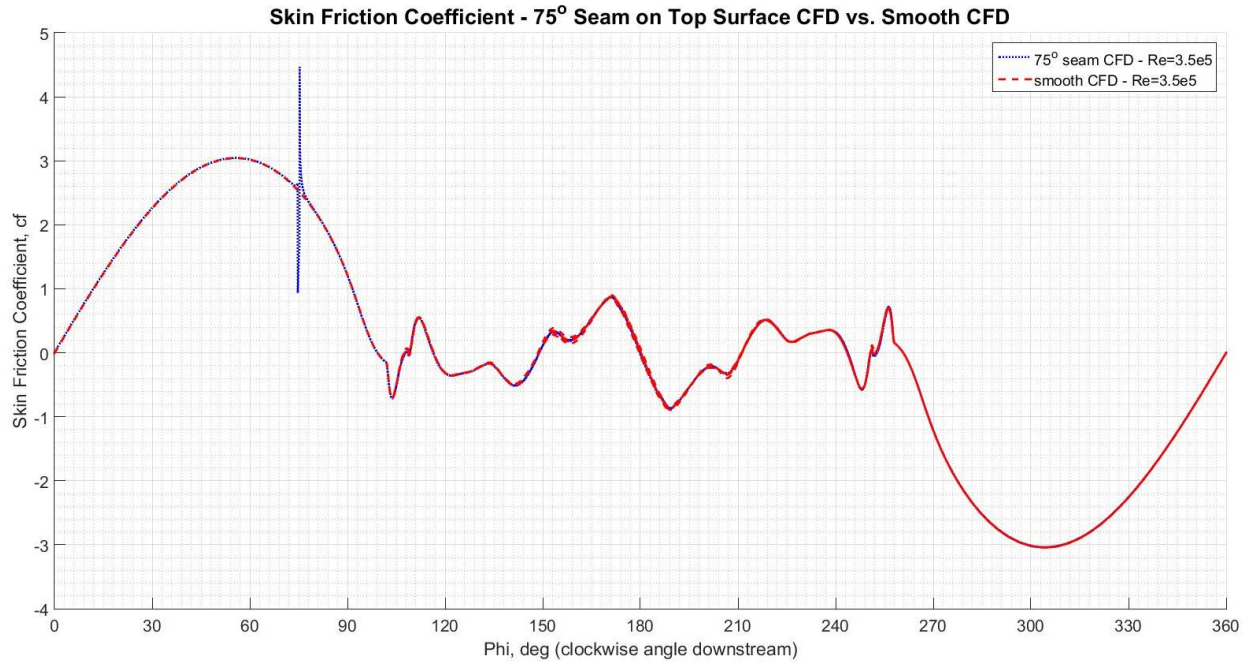
Figure 15: Skin Friction Coefficient Comparison - Single Seam at 65° (h/b=2) vs. Smooth Case CFD (Skin Friction Coefficient was normalized using the following: $cf = \frac{\tau_0}{\rho U_\infty} * \sqrt{Re}$)


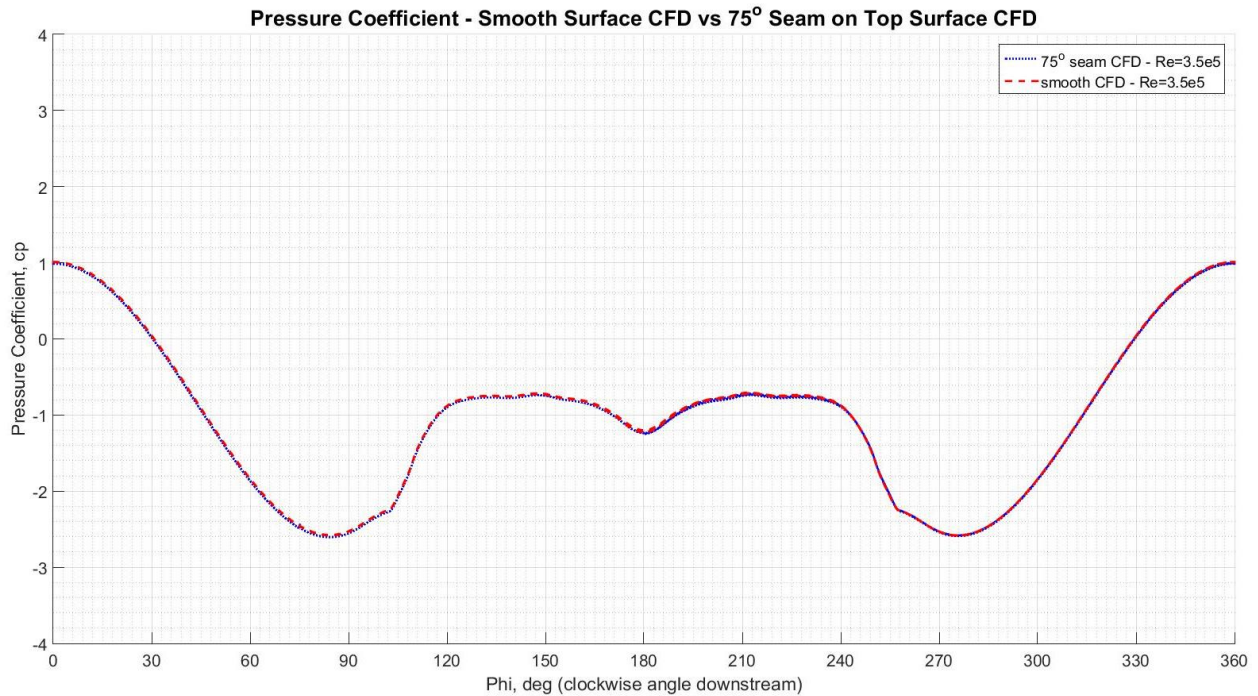*Figure 16: Pressure Coefficient Comparison - Single Seam at 65° (h/b=2) vs. Smooth Case CFD*

3.1.4   Single Seam at 75 degrees, h/b = 0.17

Due to the inconsistency with the CFD data and predicted literature effects, a second geometry with a seam was modeled. This was done to verify whether the CFD data did not appropriately capture the effects from the seam, or whether the previous case was simply not a distinct enough geometry feature for the CFD to capture. This simulation was also triangular, to match the previous case, but had a seam depth of 0.5mm and a seam width of 3 mm, giving a height to width ratio h/b = 0.17. This ratio was chosen from investigative experimental results on the height to width ratios for transverse gaps or ditches which affect boundary layer transition, with h/b = 0.17 being a ratio showing noticeable effect of speeding up the onset of boundary layer transition [12]. The figures below compare the two seam cases with differing height/width ratios (at the 75° location). It is once again observed that the CFD captures the seam geometry's effect on the boundary layer corresponding to the large spike in skin friction coefficient (and drop in pressure coefficient), however the boundary layer quickly returns to similar shape as the smooth surface case.
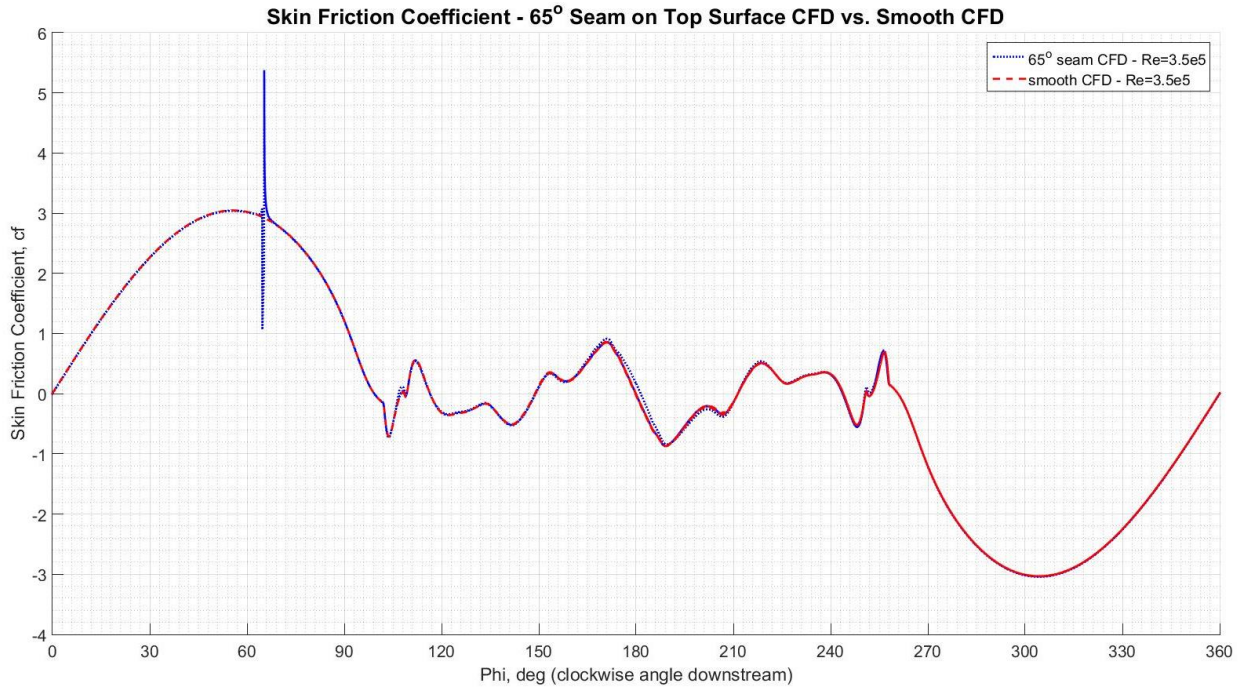

Figure 17: Skin Friction Coefficient Comparison - Single Seam h/b = 2 vs. h/b = 0.17. (Skin Friction Coefficient was normalized using the following: $cf = \frac{\tau_0}{\rho U_\infty} * \sqrt{Re}$)

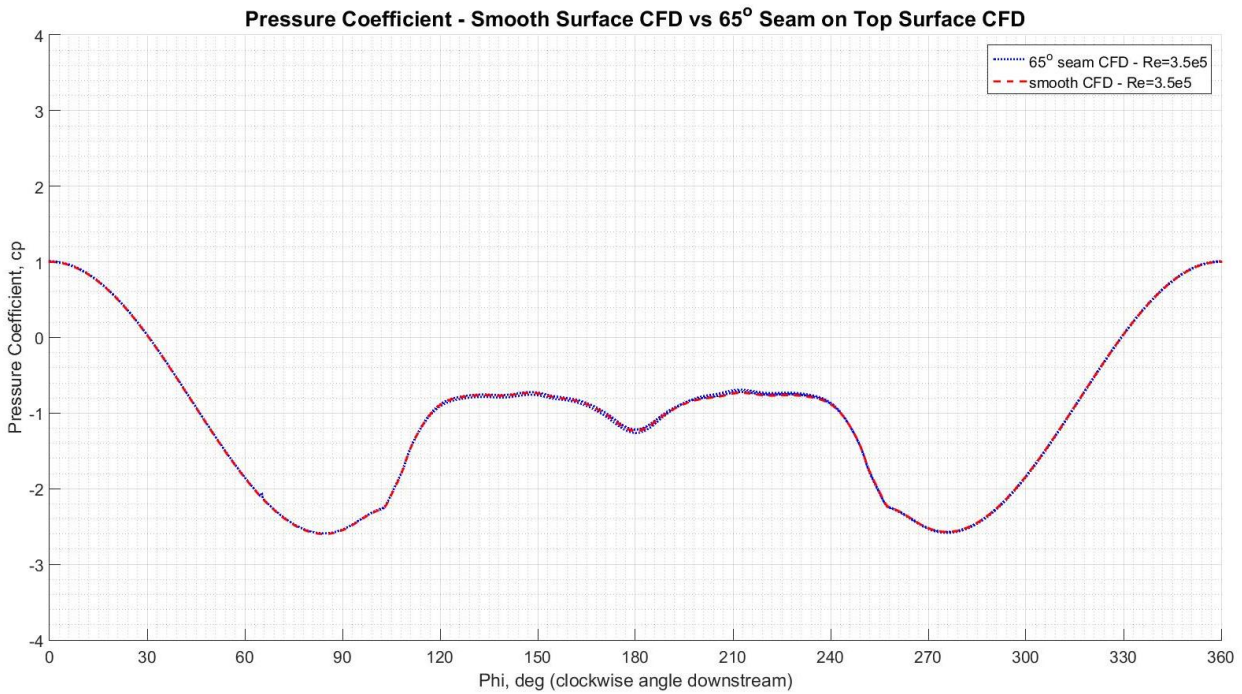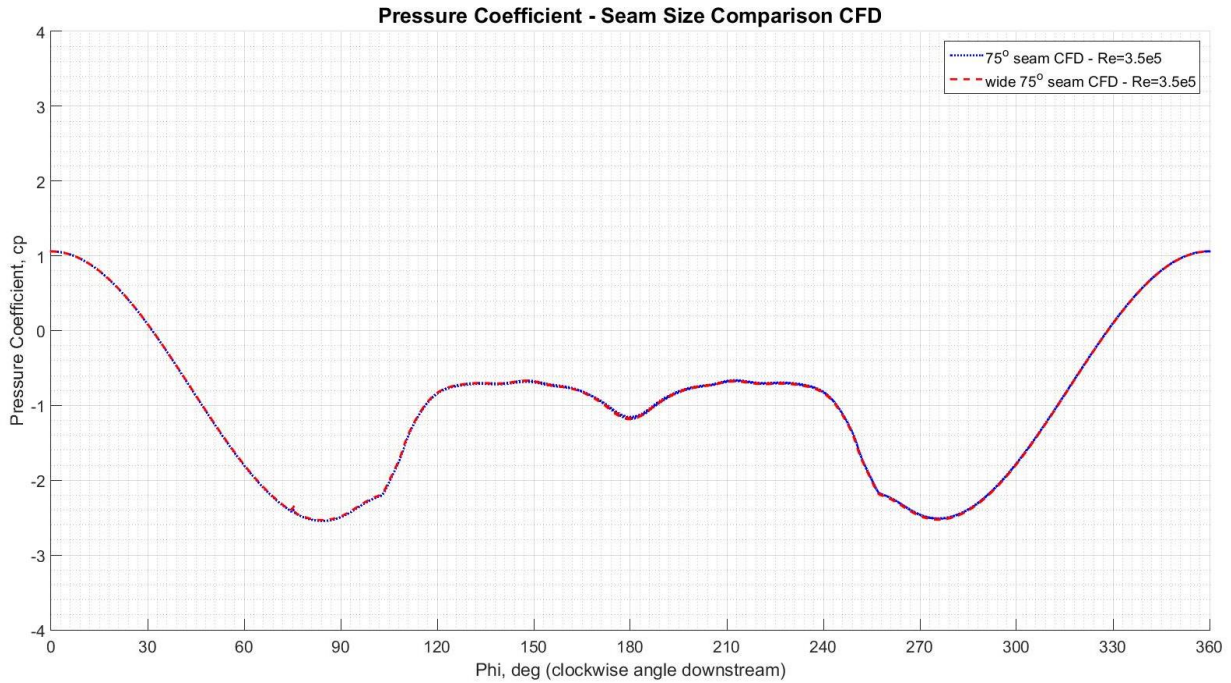*Figure 18: Pressure Coefficient Comparison - Single Seam h/b = 2 vs. h/b = 0.17*

3.2 Aerodynamic Force Coefficients

For thorough comparison with experimental data, a time history tabulation of the lift and drag coefficients was captured for both the smooth and 75seam cases. Due to the transient nature of this flow, a comparison of these coefficients was necessary to verify any temporal effects produced by the seam, such as a longer period of vortex shedding.

3.2.1 Drag Coefficient - CFD Case Comparison

The drag coefficient was recorded as a function of flow time for both the seam case and the smooth surface case. The figure shows that while the two cases approach steady-state in somewhat different structure, the steady state oscillatory value converges about the same value. Moreover, the period and amplitude of oscillation are almost identical, showing that the CFD did not capture any temporal effect from the seam which may have resulted from the expected delayed separation on the top surface.

Cd vs Flow Time - 75° Seam vs Smooth Surface

Legend:
- 75° Seam Cd time history
- 75° Seam - Cycle Time-Averaged Value: 0.698
- Smooth Surface Cd time history
- Smooth - Cycle Time-Averaged Value: 0.699
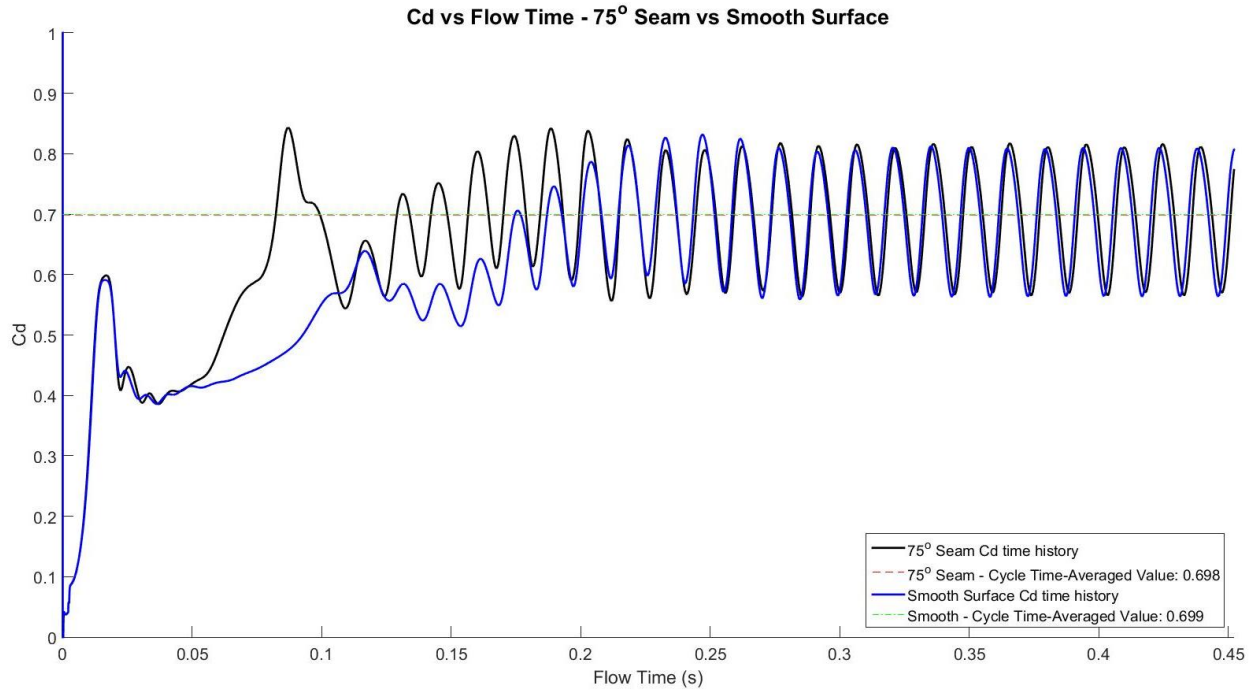
Figure 19: Drag Coefficient Convergence History Comparison - Single Seam (h/b=2) vs. Smooth Surface CFD

3.2.2   Lift Coefficient - CFD Case Comparison

Similarly, to the drag coefficient, the lift coefficient was tabulated for both the seam and smooth surface cases as a function of flow time. In this comparison, it is noted that the two cases produce a steady state oscillation about the same value, and the period and amplitude of oscillation are almost identical. It is clear from the figure that the time history plots are out of phase in time, however, due to the negligible effects seen in other value comparisons, it cannot be concluded that the seam produced this effect.

Cl vs Flow Time - 75° Seam vs Smooth Surface

Cl

Flow Time (s)

75° Seam Cl time history
75° Seam - Cycle Time-Averaged Value: 0.003
Smooth Surface Cl time history
Smooth - Cycle Time-Averaged Value: 0.007
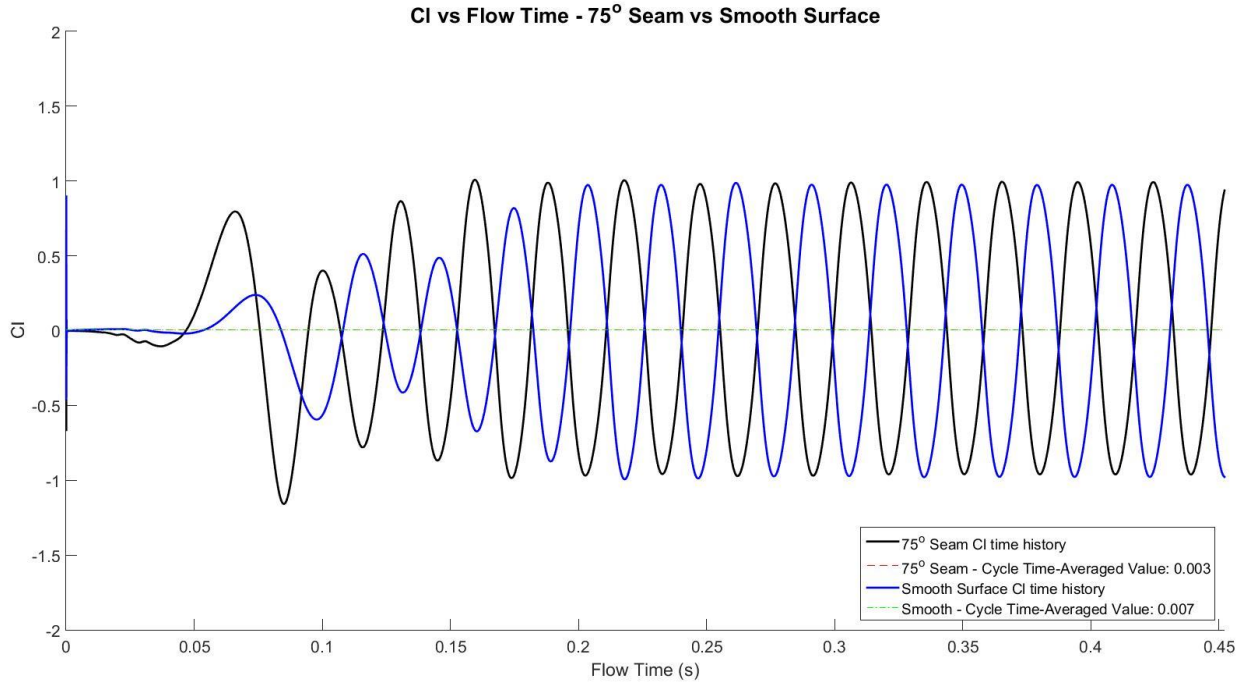
Figure 20: Lift Coefficient Convergence History Comparison - Single Seam (h/b=2) vs. Smooth Surface CFD

3.2.3   Force Coefficients – Experimental Data

Both the drag and lift coefficients recorded were compared with experimental data available for the Reynolds number examined in this study. The drag coefficient was compared to experimental results for smooth surface cylinders in crossflow, as seen in the figure below. The CFD results show good agreement with experimental values, although it is noted that the Reynolds number selected is in or around the transition region, making values in this area much harder to define specifically. The reasoning behind the selection of the Reynolds number of this study was for comparison to experimental results for a cylinder with a single seam, examined in the lift coefficient comparison in the following figure.

Drag Coefficient - Experimental Data vs CFD
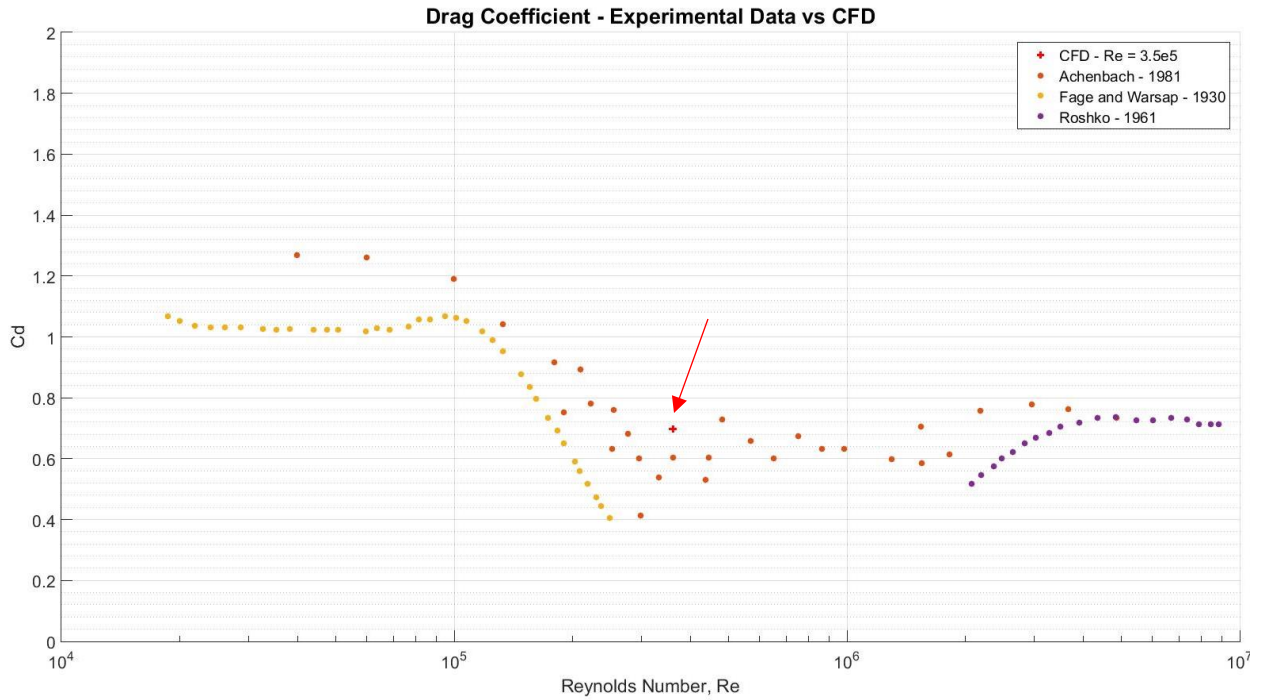
Figure 21: Drag Coefficient for Several Wind Tunnel Tests vs. CFD time averaged value

The lift coefficient was compared to experimental data from the study previously mentioned, by Hong et. al 2015 [32], which took a cylinder with a single seam and rotated the cylinder in 15-degree increments from 0 degrees (front stagnation point), to 150 degrees. The lift force was documented at each 15-degree increment, and a noticeable negative (or downward) lift force began to arise at the 60 degree mark, with the most prominent force at 75 degrees, as seen in the figure below. The next data

Figure 22: Observed Lift Force as Cylinder was Rotated for CFD Lift Coefficient Validation [32]
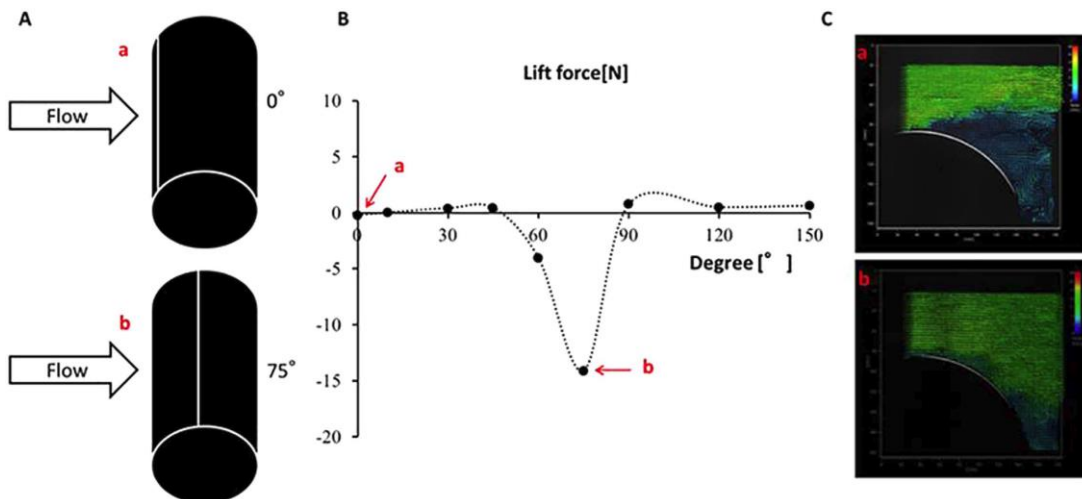
point in the experiment was at 90 degrees, and therefore it is unclear whether there are intermediate

values between 75 and 90 degrees where the lift force was downward. As stated previously, a secondary

seam location of 65 degrees was chosen due to the documented downward lift force at 60 degree and 75

degree seam locations, and a negative trend in the observed data.

The flow conditions used for that study were replicated for this one to draw comparisons between

experimental and CFD results, and the lift force registered in the experimental study was converted to a

lift coefficient using $cl = \frac{L}{\frac{1}{2}\rho U_\infty{}^2 A}$, where A represented the projected area of the cylinder, with diameter of

220mm (characteristic length) and unit width [32]. A similar calculation was used for the CFD results and

the comparison can be seen in the figure below. The CFD results did not capture the large increase in

downward lift force as the experimental results did, which is consistent with the results mentioned

previously, where the CFD did not appear to capture the delayed separation predicted by the seam on the
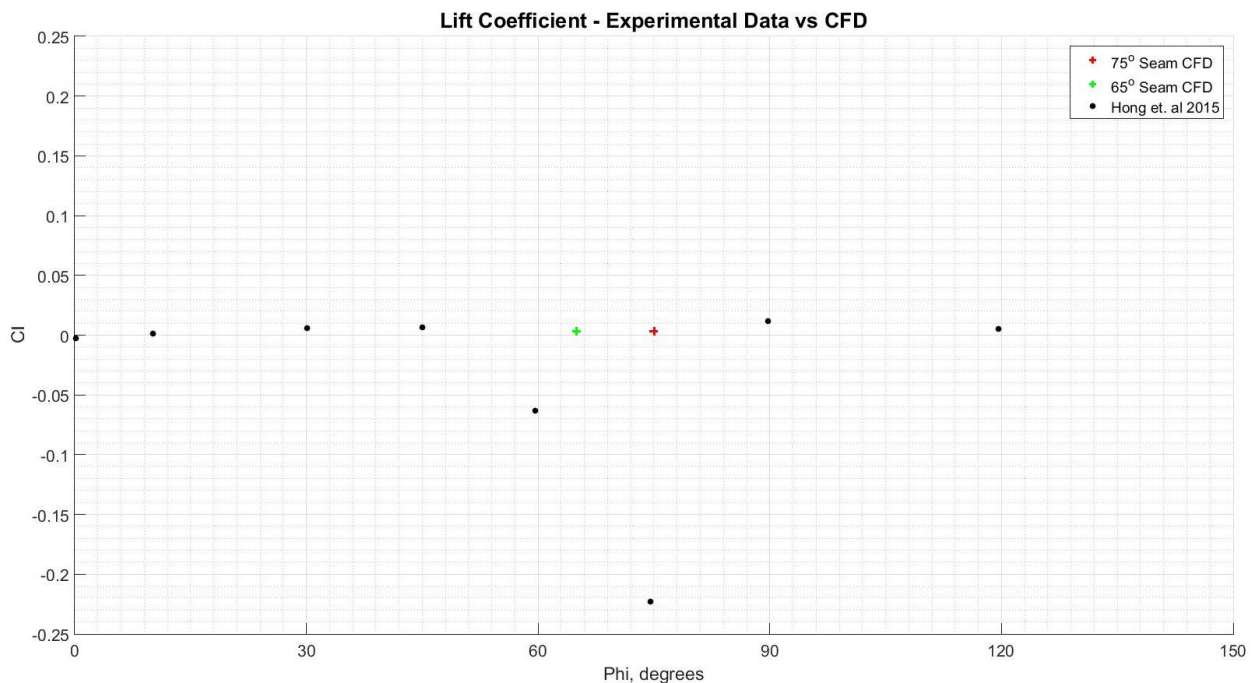
top surface.

Figure 23: Lift Coefficient (calculated from Hong et. al 2015) vs. CFD time averaged lift coefficient values

3.3 Grid Independence Study

The numerical discretization error was characterized using the procedure detailed in Appendix A from the ASME Journal of Fluids Engineering Editorial Policy Statement on the control of Numerical Accuracy [47]. The step-by-step analysis was conducted using the solution values for the Drag Coefficient, due to its use in comparison to experimental data and thus an appropriate calculated value of interest for validation purposes. The grid spacing used in this study from the coarsest grid to the finest grid was not uniform due to memory limitations for conducting the finest grid. In addition, the solution value for Drag Coefficient was extremely close between the medium grid to the finest grid, leading the author to conclude that the mesh was refined enough at the medium grid level in converging to the "exact" numerical solution.

However, when conducting the numerical discretization error procedure as detailed in Appendix A, the methodology would not converge onto a specific order of accuracy for the apparent order, p, as referenced in Section 2.2.5 Grid Independence Study/Validation. The fixed-point iteration would diverge and not produce a logical value for p. The author suggests that the reason for this results from the issue with the similar solution values for the medium and fine grid and the number of cells for both grids being very close as well. In the procedure, it is noted that if the difference between solution values of successive grids is "very close" to zero, the [procedure] doesn't work [47]. Additionally, it's theorized that the "exact" solution has been attained, and if possible, calculations with additional grid refinement may be performed; if not, the results may be reported as such [47]. In the case of this study, a more refined grid could not be performed due to the computational resource limitations. Therefore, for the fine grid solution, assumed p values ranging from 0.75 to 2 were used to obtain associated error percentages with solutions critiqued on that order of error, the results of which are tabulated below:

Error	Apparent order p (through fixed-point iterative solution)									
Value	0.7	1	1.25	1.5	1.75	2	2.25	2.5	2.75	3
$\varphi_{ext}{}^{21}$	0.6773	0.6829	0.6863	0.6886	0.6902	0.6914	0.6924	0.6931	0.6938	0.6943
$e_a{}^{21}$	1.5%	1.5%	1.5%	1.5%	1.5%	1.5%	1.5%	1.5%	1.5%	1.5%
$e_{ext}{}^{21}$	3.27%	2.42%	1.91%	1.57%	1.34%	1.16%	1.02%	0.91%	0.82%	0.75%

GCI_{fine} [21]	3.96%	2.95%	2.34%	1.94%	1.65%	1.43%	1.26%	1.13%	1.02%	0.92%

The calculated error associated with the Grid Convergence Index for each value of p was plotted as error bars on the extrapolated value, and the fine grid solution was found to fall within the error bars of even the tightest margin of error for the extrapolated value with the associated GCI error percentage, as seen in Figure 24.

Figure 24: Numerical Discretization Error - Fine Grid Solution for Drag Coefficient
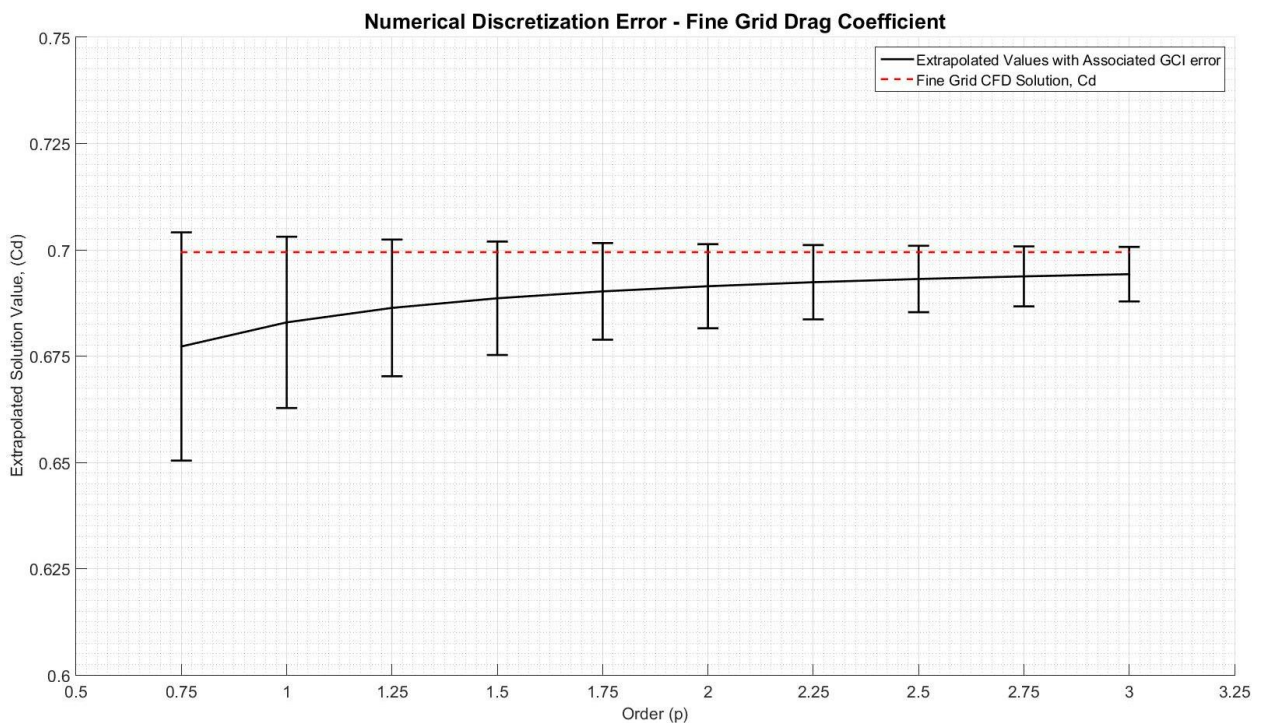
3.4 Flow Visualizations

3.4.1   Contour and Vector Plots

In this section, several flow visualizations are displayed to give an illustrative view of the aerodynamics present in this flow. Contours of velocity magnitude for the entire wake region are shown to display the vortex shedding found at this Reynolds number. A closer look at the region near the surface with a single seam is examined through velocity contours and velocity vector plots to show that the natural boundary layer transition is captured, with the formation of a separation bubble.

Figure 25: Velocity Contour Plot at Converged Solution for Single Seam (h/b=2) CFD Simulation Displaying Large Scale Vortex Shedding Phenomenon
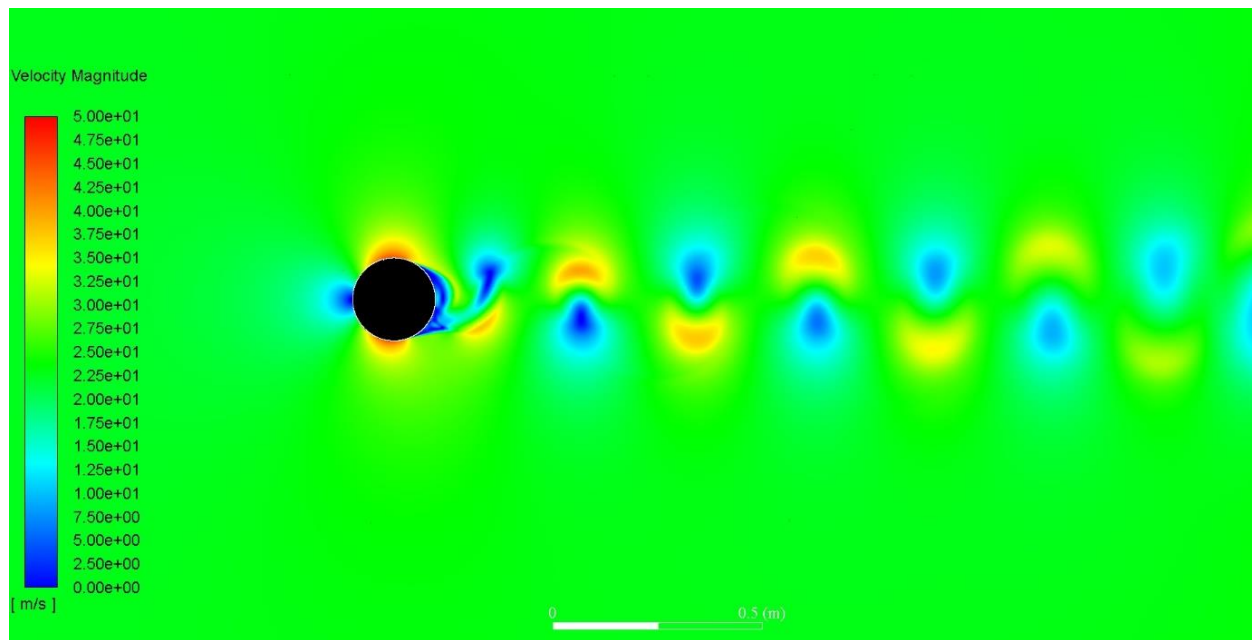
Figure 26: Inset of Velocity Contour Plot Converged Solution for Single Seam (h/b=2) CFD Simulation Displaying Seam and Boundary Layer Separation Region
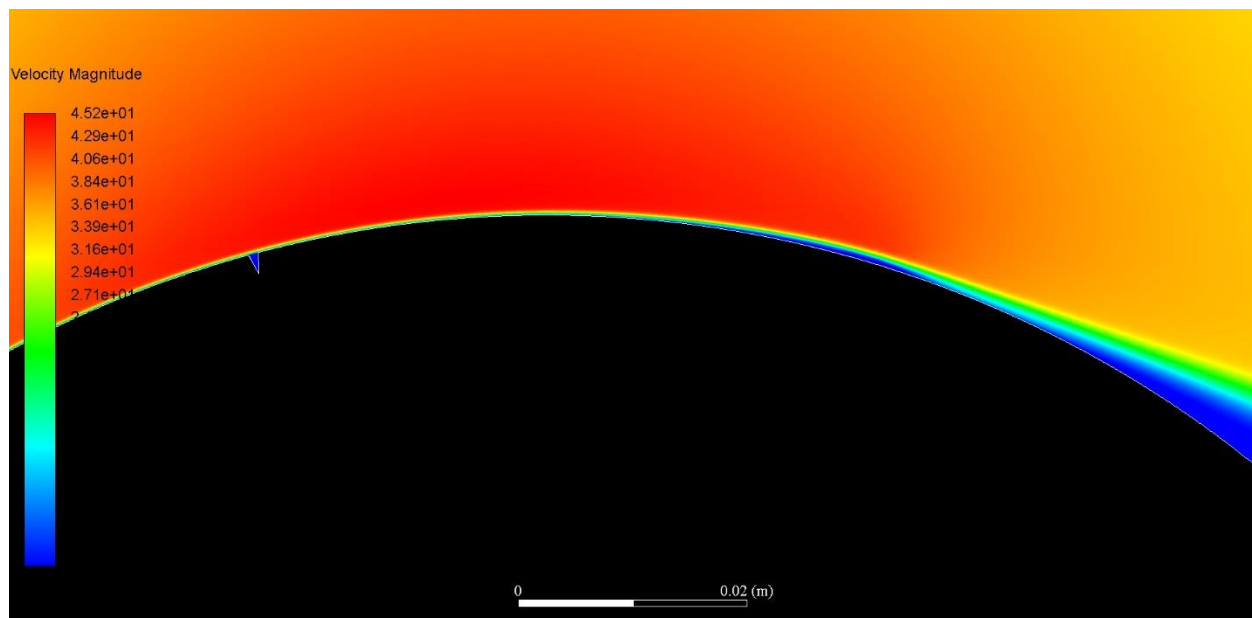
The formation of a separation bubble is thoroughly documented in literature for cylinders to occur at and around the Reynolds number of this study, which translates to the transition region of the boundary layer from laminar to turbulent [2,6,48]. In one of the first works to diagram the separation bubble, seen in

Figure 28, a direct comparison can be made to the velocity vector plot shown in the CFD simulation in

Figure 27. The existence of the separation bubble is corroborated in the pressure contour plot seen in

Figure 14, where the pressure value is delayed in retreating toward a stagnant value. This is also

displayed in the work by Horton [33], as seen in Figure 29, further supporting the ability for the CFD

simulation to model the boundary layer transition accurately. However, the effect of the seam, as

predicted by literature, to delay the final separation point, is not observed, nor the effects that would follow

this phenomenon.

Figure 27: Velocity Vector Plot at Converged Solution for Single Seam (h/b=2) CFD Simulation Displaying Separation Bubble Formed during Boundary Layer Transition

FIG. 2a. SECTIONAL VIEW OF A TWO-DIMENSIONAL SHORT LAMINAR SEPARATION BUBBLE. (Z SCALE MUCH EXAGGERATED).
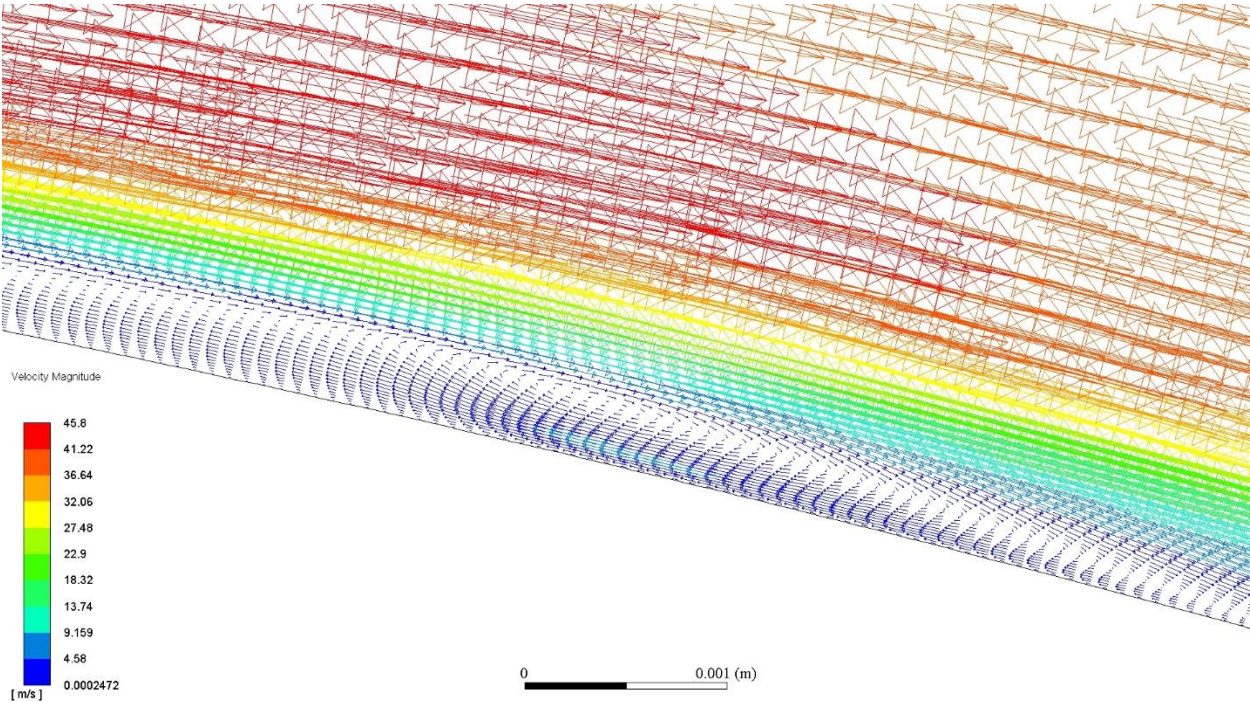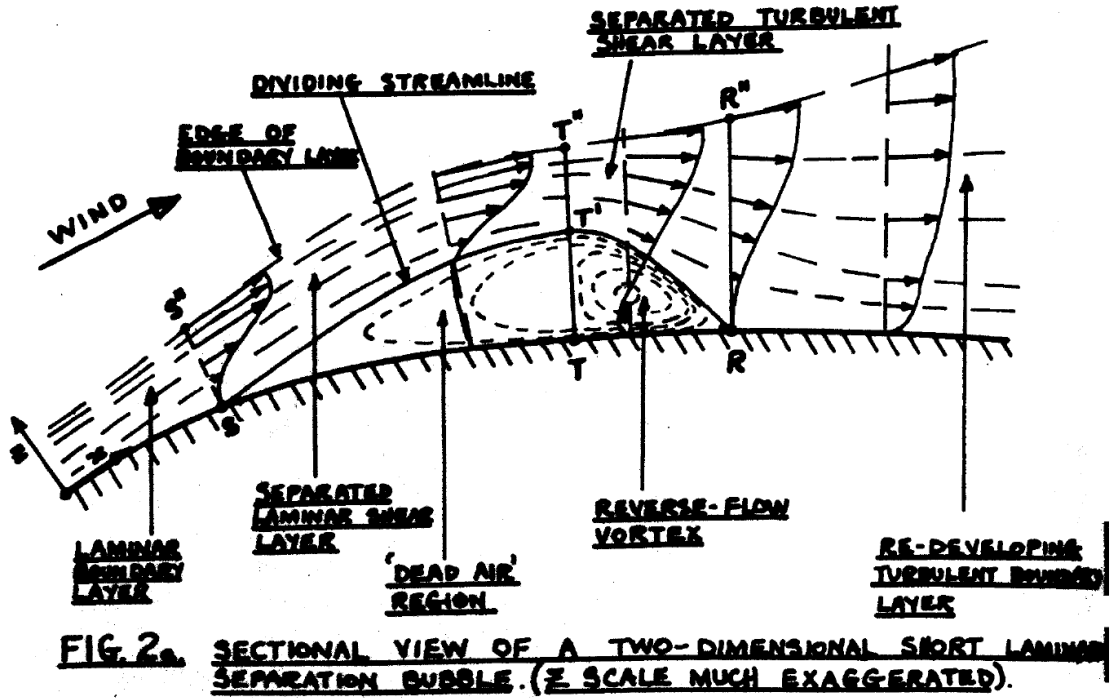
Figure 28: From Laminar Separation Bubbles in Two- and Three-Dimensional Incompressible Flow, H. P. Horton, 1968
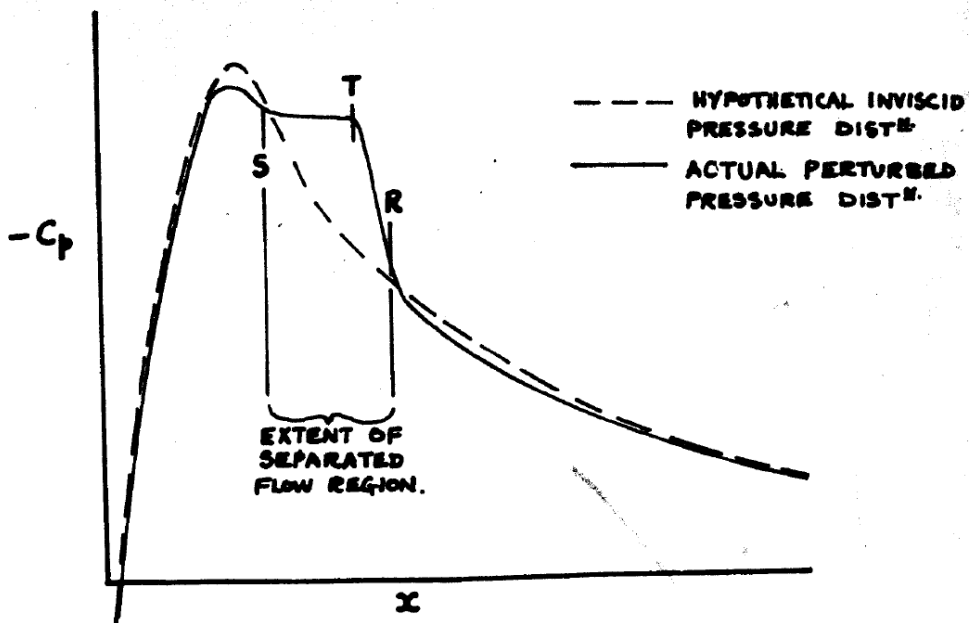
Figure 29: From Laminar Separation Bubbles in Two- and Three-Dimensional Incompressible Flow, H. P. Horton, 1968

3.4.2 Transient Flow Structure Animations

The following figures display contours of Vorticity on a log scale to better visualize the vortex shedding phenomenon. The period from frame to frame corresponds to a flow time of 0.45 seconds. If the effects of the seam as predicted by literature were captured, a delayed separation caused by the seam on the top surface would influence the period and consistency of the vortex shedding due to the asymmetry it would create. However, as stated previously, because the delayed separation on the top surface was not captured in the CFD results, the vortex shedding structure is identical to that of a smooth surface.

Figure 30: Time Series of Vorticity Displaying the Vortex Shedding Phenomenon. (Time between images is 450ms)
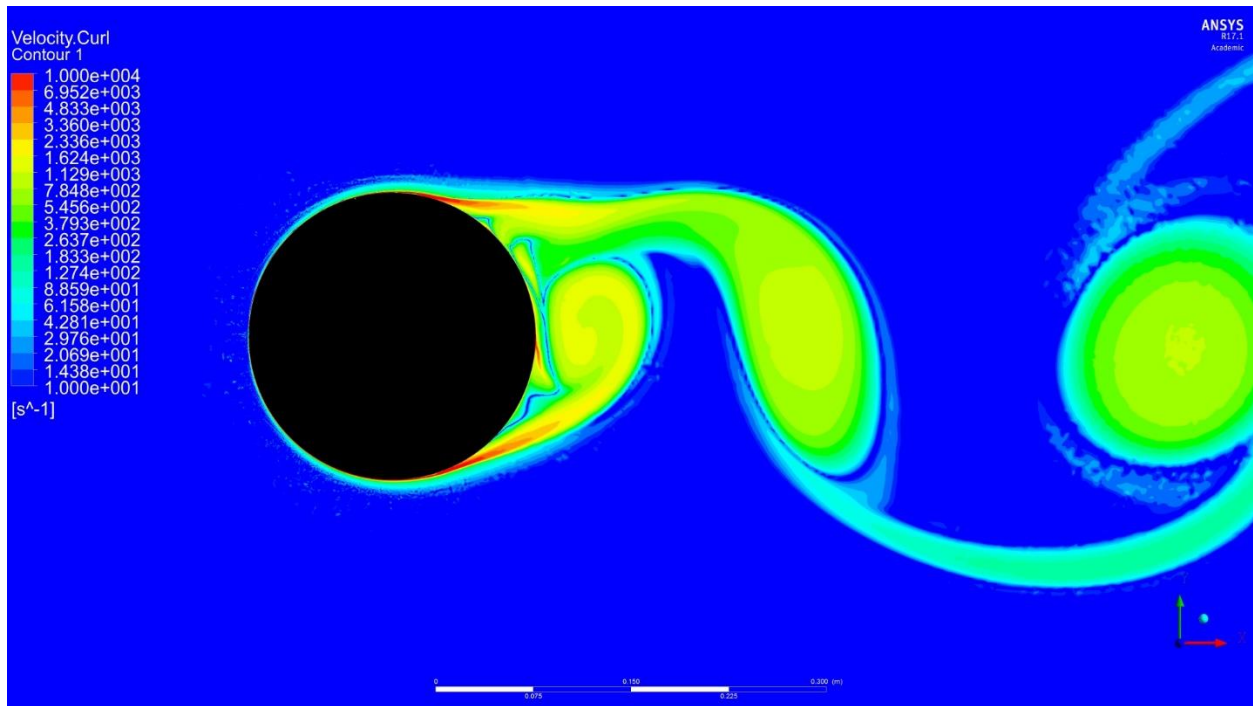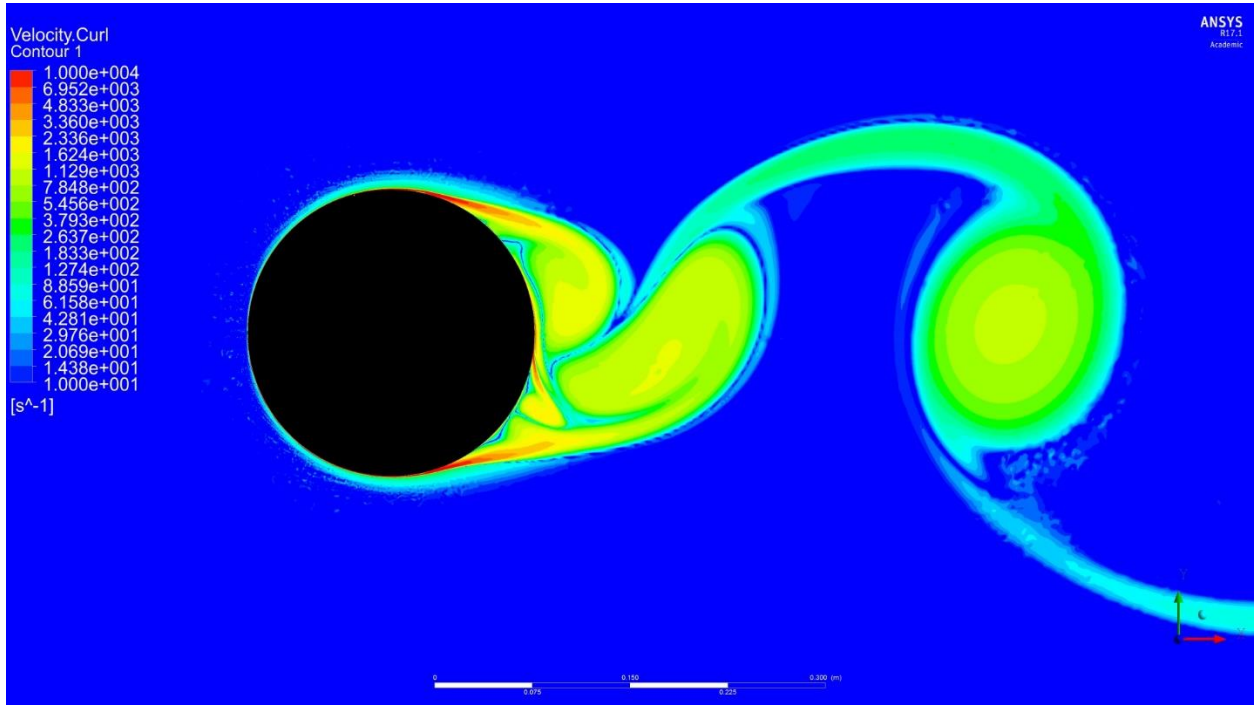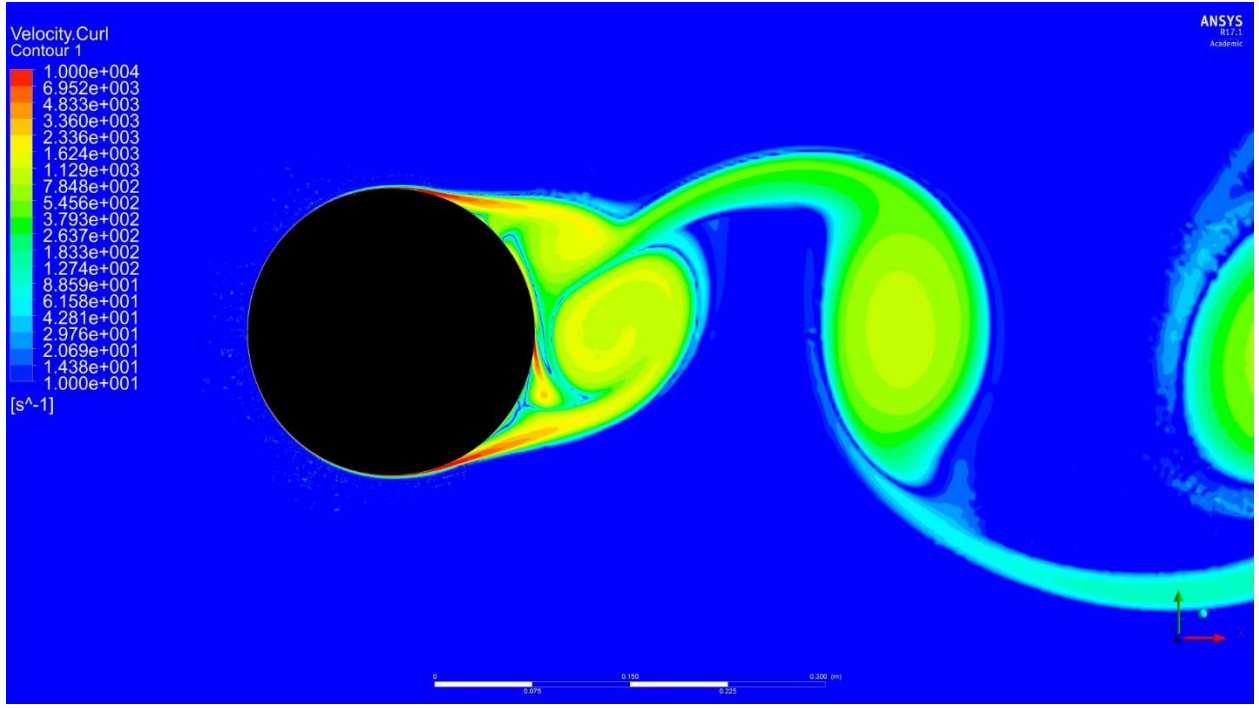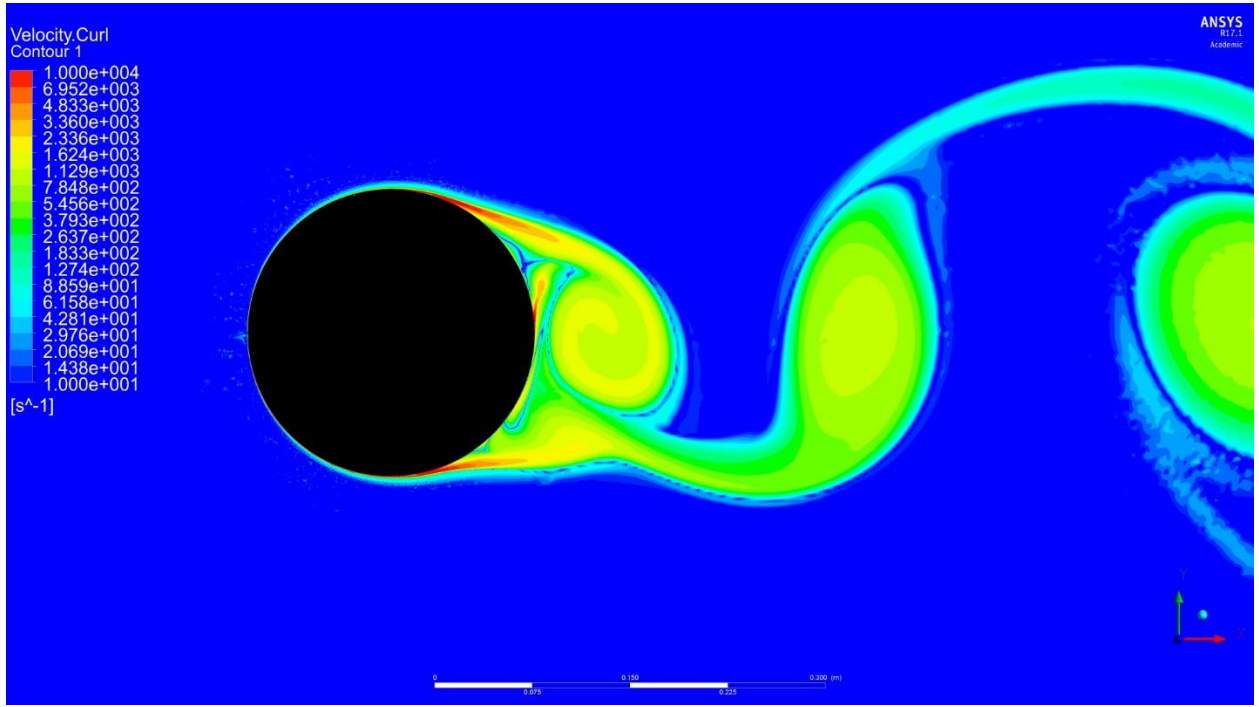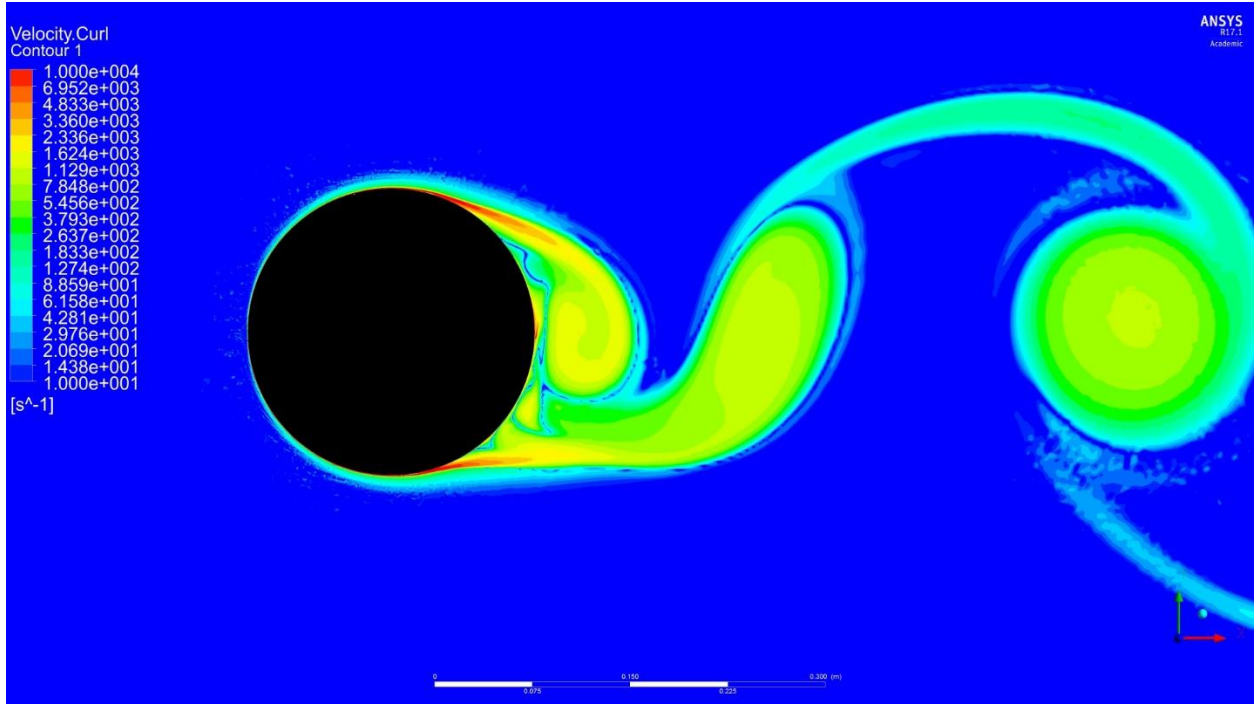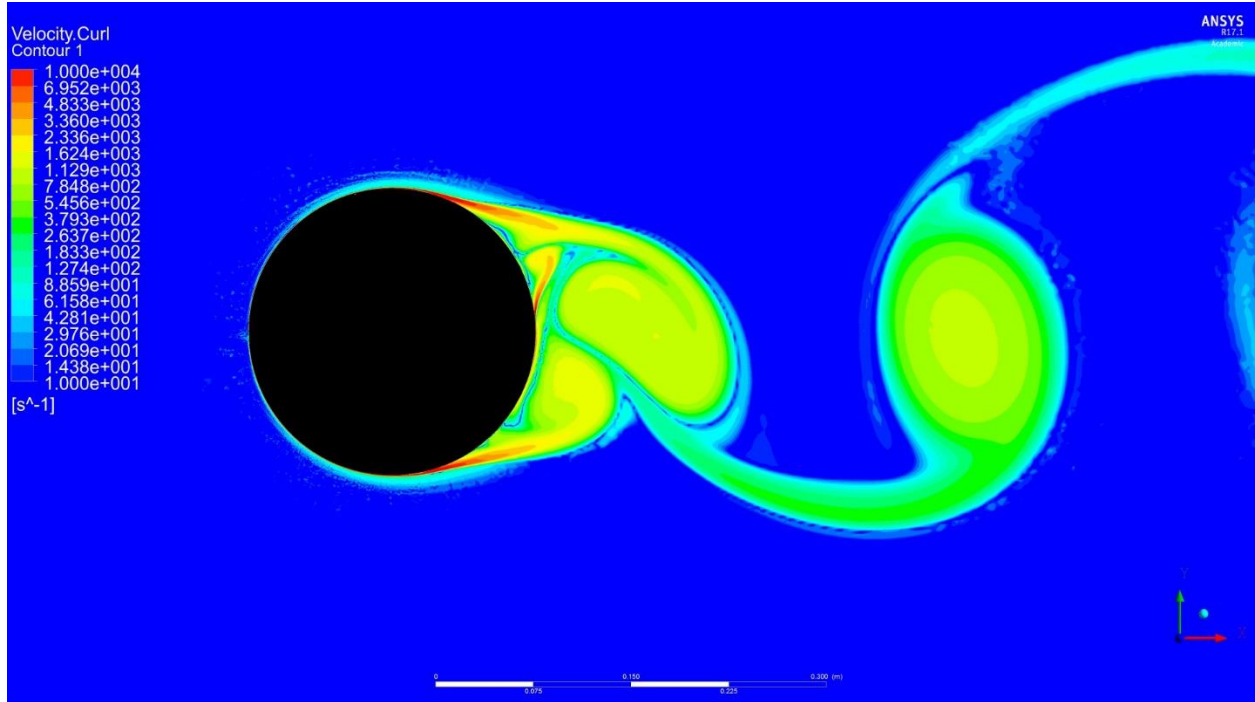
4   DISCUSSION AND CONCLUSIONS

An applied computational fluid dynamics approach was taken to analyze the aerodynamic effects of the seams on the surface of a soccer ball. A two-dimensional representation of a single seam was translated into computational space as a cylinder with a single seam in cross-flow. The goal of this study was to analyze the feasibility and accuracy of a computational approach using a transition-based solver in capturing the effects that the seam has on boundary layer transition, flow separation point, and wake structure. An auxiliary goal was to develop a computational analysis framework for which future work could expand upon to fill the gap of computational data which complements experimental data and trajectory analyses.

The first goal was rigorously pursued but not entirely achieved. A large portion of this work focused on developing the methodology to appropriately apply a transition-based solver to the flow conditions investigated. As noted in Section 2, there were many mistakes made along the way, which proved to help define an accurate methodology. This included the meshing strategy, computational solver selection, solver tuning, and data analysis methods. Extrapolating from previous computational work, experimental data gathering practices, and some trial and error, the final methodology used in this study was concluded given the resources available.

With a thorough examination of the comparisons between experimental data and CFD results in the previous section, several deductions can be made. First, the results do not indicate that the seam had any effect on the flow physics, as the results for the smooth surface and seam cases were practically identical. This is displayed through the comparisons of skin friction, pressure, drag, and lift coefficients as well as flow visualizations. Second, the results indicate that the CFD results show the seam geometry was captured, shown in the spike after the seam in the skin friction coefficient data, similarly seen in flat plate and other related analyses of transverse gaps and ditches [12,41]. However, the downstream effects of the seam did not materialize, as predicted by literature, as all the subsequent data shows similar results to that of the smooth surface case.

Downstream from the seam, the separated region has large fluctuations in skin friction, which did not correlate directly to physical phenomena. Initially, it was thought that the time-averaging technique

used was the cause of this discrepancy. To confirm whether this was the case, all of the timesteps in the converged solution were plotted against the time-averaged solution used in this study and the global time-averaged solution, which averaged the data over the entire converged time domain.

Figure 31: Investigation into Separated Region Skin Friction Coefficient Fluctuations. Comparison of Instantaneous Time-Step Data vs. Vortex Shedding Cycle Averaged and Global Time Averaged Values (Skin Friction Coefficient was normalized using the following: $cf = \frac{\tau_0}{\rho U_\infty} * \sqrt{Re}$)
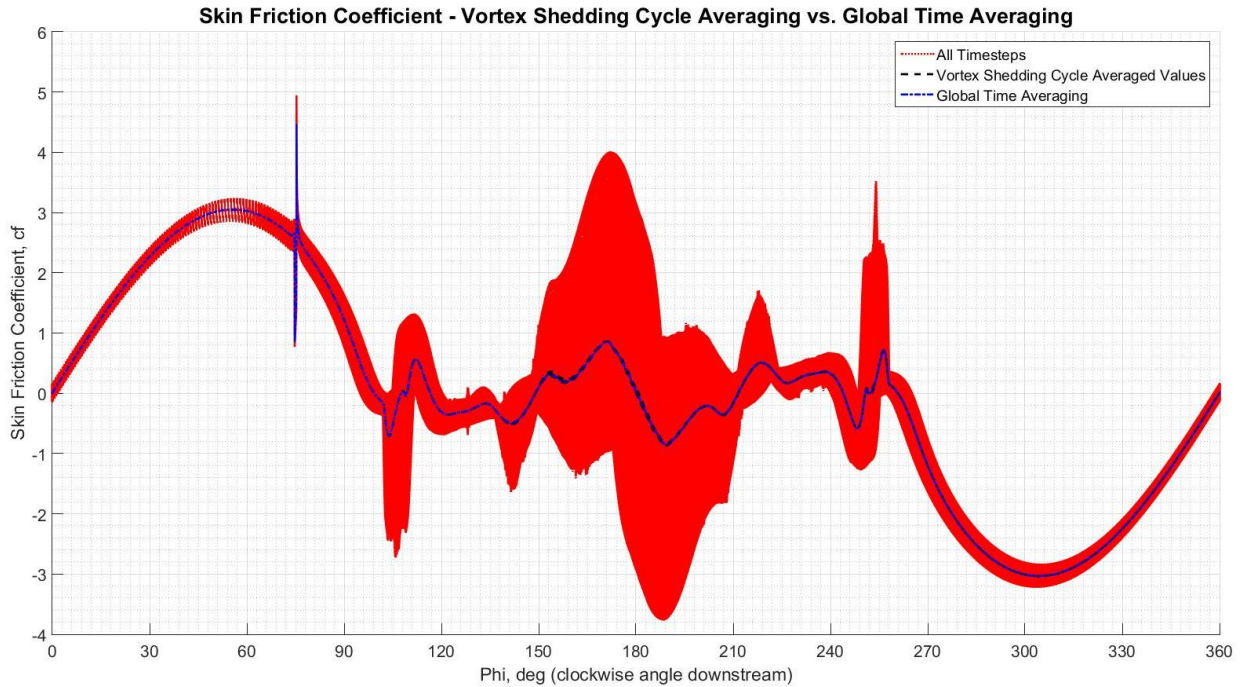
Upon investigation of this data, the author found that the inconsistency in the separated region in the CFD results may have materialized due the unrealistic calculation of a complete boundary layer in the separated region, caused by the uniform refined grid spacing used to capture the boundary layer in the attached region. More refined cells used to ensure accurate calculation of the boundary layer in the attached region may have inadvertently caused mesh-induced, increased wall shear stress calculated in the separated region, not seen in experimental data. A recommendation for future work would be to include using a scale resolving solution criteria, where the Transition SST model can be coupled with a delayed eddy simulation (DES) solver to shield the boundary layer from the free stream flow to more accurately model that region [7]. These results, coupled with the inconsistencies in the pressure, lift, and

drag data, lead the author to conclude that the primary goal was not achieved, as the effects of a single seam were not captured as predicted by experimental work.

The auxiliary goal was achieved as the author has attempted to provide a baseline for which future work can expand upon. The type of flow under examination, as well as the scale of the geometry feature (the seam) relative to the body under study (soccer ball), contribute to the difficulty in developing accurate computational results. The availability of computational resources in future work shows promise in defining much more accurate computational results than for this study. However, the framework developed in this study can guide future research both experimentally and computationally.

There are several other suggestions for which future work may expand. One of which includes the transition to a three-dimensional analysis, due to the induced effects of three-dimensional flow structures as well as asymmetric geometry features. This is especially important when analyzing a body such as the soccer ball which is spherical, and therefore not necessarily symmetric about the span-wise axis as the current study assumed. Further, more experimental work is suggested in the realm of single-seam or single geometry feature bodies to accompany and validate CFD results. At the time of this paper, the only known work which sought to tabulate experimental data on a sphere with a single seam was not yet published [55]. With a robust methodology and targeted application of the resources, a computational solution can accompany experimental results to give a clearer picture of the interesting and complex flow phenomenon investigated in this study.

REFERENCES

[1] E. Achenbach, "Distribution of Local Pressure and Skin Friction Around a Circular Cylinder in Cross-Flow up to Re=5x10^6"," *Journal of Fluid Mechanics,* vol. 34, pp. 625-639, 1968.

[2] J. C. K. Cheung and W. H. Melbourne, "Effects of Surface Roughness on a Circular Cylinder in Supercritical Turbulent Flow," in *Australasian Fluid Mechanics Conference*, 1995.

[3] A. Roshko, "Experiments on the Flow Past a Circular Cylinder at Very High Reynolds Number"," 1960.

[4] E. Achenbach, "Influence of Surface Roughness on the Cross-Flow Around a Circular Cylinder," *Journal of Fluid Mechanics,* vol. 46, pp. 321-335, 1971.

[5] E. Achenbach and E. Heinecke, "On Vortex Shedding from Smooth and Rough Cylinders in the Range of Reynolds Numbers 6x10^3 to 5x10^6"," *Journal of Fluid Mechanics,* vol. 109, pp. 239-251, 1981.

[6] A. Fage and J. H. Warsap, "The Effects of Turbulence and Surface Roughness on the Drag of a Circular Cylinder," 1929.

[7] S. Hong, T. Asai and K. Seo, "Visualization of Air Flow Around Soccer Ball Using a Particle Image Velocimetry," Scientific reports, 2015.

[8] J. H. Lienhard, "Synopsis of Lift, Drag, and Vortex Frequency Data for Rigid, Circular Cylinders," Technical Extension Service, 1966.

[9] E. Achenbach, "Vortex Shedding from Spheres," *Journal of Fluid Mechanics,* vol. 62, no. 2, pp. 209-221, January 1974.

[10] E. Achenbach, "Experiments on the Flow Past Spheres at Very High Reynolds Numbers," *Journal of Fluid Mechanics,* vol. 54, pp. 565-575, 1972.

[11] M. e. a. Passmore, "The Aerodynamic Performance of a Range of FIFA-approved Footballs," Proceedings of the Institution of Mechanical Engineers, Part P: Journal of Sports Engineering and Technology, 2012.

[12] J. E. Goff, T. Asai and S. Hong, "A Comparison of Jabulani and Brazuca non-spin Aerodynamics," Proceedings of the Institution of Mechanical Engineers, Part P: Journal of Sports Engineering and Technology, 2014.

[13] E. Kellis and A. Katis, "Biomechanical Characteristics and Determinants of Instep Soccer Kick," *Journal of Sports Science and Medicine,* pp. 6, 154-165, 2007.

[14] S. Hong and T. Asai, "Effect of Panel Shape of Soccer Ball on its Flight Characteristics," Scientific Reports 4: 5068, 2014.

[15] T. Asai and K. Kamemoto, "Flow Structure of Knuckling Effect in Footballs," *Journal of Fluids and Structures,* vol. 27, no. 5, pp. 727-733, 2011.

[16] S. Hong, T. Asai and K. Seo, "Flow Visualization Around Panel Shapes of Soccer Balls," in *7th Asia-Pacific Congress on Sports Technology*, 2015.

[17] T. Asai, O. Kobayashi and R. Sakashita, "Fundamental Aerodynamics of the Soccer Ball," International Sports Engineering Association, 2007.

[18] J. W. M. Bush, "The Aerodynamics of the Beautiful Game," Department of Mathematics, MIT, 2013.

[19] S. Barber and M. J. Carre, "The Effect of Surface Geometry on Soccer Ball Trajectories," International Sports Engineering Association, 2010.

[20] M. J. Carre and S. Barber, "A Novel Sports Ball Aerodynamics Tool: Soccer Ball Design," Sports Technology, 2012.

[21] J. E. Goff, "A Review of Recent Research into Aerodynamics of Sport Projectiles," International Sports Engineering Association, 2013.

[22] S. J. Haake, S. R. Goodwill and M. J. Carre, "A New Measure of Roughness for Defining the Aerodynamic Performance of Sports Balls," in *Proceedings of the Institution of Mechanical Engineers Part C: Journal of Mechanical Engineering Science*, 2007.

[23] K. L. Suder, J. E. O'Brien and E. Reshotko, "Experimental Study of Bypass Transition in a Boundary Layer," NASA-TM-100913, 1988.

[24] B. D. Texier, C. Cohen, D. Quere and C. Clanet, "Physics of Knuckleballs," *New Journal of Physics,* 2016.

[25] R. D. Mehta, "Sports Ball Aerodynamics," 2009.

[26] C. Clanet, "Sports Ballistics," *Annual Review of Fluid Mechanics,* pp. 47:455-78, 2015.

[27] J. E. Goff and M. J. Carre, "Trajectory Analysis of a Soccer Ball," *American Journal of Physics,* vol. 77, no. 11, pp. 1020-1027, 2009.

[28] R. K. Hanna'a, "CFD in Sport - A Retrospective; 1992-2012," in *9th Conference of the International Sports Engineering Assocation*, 2012.

[29] M. e. a. Passmore, "Experimental Sutdies of the Aerodynamics of Spinning and Stationary Footballs," 2007.

[30] P. Jalilian, P. K. Kreun, M. M. Makhmalbaf and W. W. Liou, "Computational Aerodynamics of Baseball, Soccer Ball and Volleyball," *American Journal of Sports Science,* vol. 2, no. 5, pp. 115-121, 2014.

[31] V. Krishnan, K. D. Squires and J. R. Forsythe, "Prediction of the Flow Around a Circular Cylinder at High Reynolds Number," in *44th AIAA Aerospace Sciences Meeting and Exhibit*, 2006.

[32] G. Vaz, C. Mabilat, R. van der Wal and P. Gallagher, "Viscous Flow Computations on Smooth Cylinders: A Detailed Numerical Study with Validation," in *26th International Conference on Offshore Mechanics and Arctic Engineering*, 2007.

[33] S. Barber, S. B. Chin and M. J. Carre, "Sports Ball Aerodynamics: A Numerical Study of the Erratic Motion of Soccer Balls," *Computers and Fluids,* pp. 1091-1100, 2009.

[34] R. H. Pletcher, J. C. Tannehill and D. A. Anderson, Computational Fluid Mechanics and Heat Transfer, Third ed., CRC Press, 2013, pp. 247-314.

[35] "The History of the Official World Cup Match Balls," [Online]. Available: htttp://www.soccerballworldcom/HistoryWCBalls.htm.

[36] J. E. Goff, S. Hong and T. Asai, "Aerodynamic and Surace Comparisons between Telstar 18 and Brazuca," 2018.

[37] J. P. Nenni and G. L. Gluyas, "Aerodynamic Design and Analysis of an LFC Surface," *Astronautics and Aeronautics,* vol. 4, no. 7, pp. 52-57, 1966.

[38] S. Hong and T. Asai, "Aerodynamic Effects of Dimples on Soccer Ball Surfaces," *Heliyon,* 2017.

[39] M. Forte, J. Perraud, A. Seraudie, S. Beguet, L. Gentili and G. Casalis, "Experimental and Numerical Study of the Effects of Gaps on Laminar Turbulent Transition of Incrompressible Boundary Layers," in *IUTAM_ABCM Symposium on Laminar Trubulent Transition*, 2015.

[40] S. Beguet, J. Perraud, M. Forte and J. -P. Brazier, "Modeling of Transverse Gaps Effects on Boundary-Layer Transition," *Journal of Aircraft,* vol. 54, no. 2, 2017.

[41] H. P. Horton, "Laminar Separation Bubbles in Two and Three Dimensional Incompressible Flow," University of London, 1968.

[42] M. Gaster, "The Structure and Behaviour of Laminar Separation Bubbles," Aeronautical Research Council, 1969.

[43] P. J. Roache, K. N. Ghia and F. M. White, "Editorial Policy Statement on the Control of Numerical Accuracy," *Journal of Fluids Engineering,* 1986.

[44] P. J. Roache, "Perspective: A Method for Uniform Reporting of Grid Refinement Studies," *Journal of Fluids Engineering,* vol. 116, pp. 405-413, 1994.

[45] P. J. Roache, "Quantification of Uncertainty in Computational Fluid Dynamics," *Annual Review Fluid Mechanics,* pp. 29:123-60, 1997.

[46] F. R. Menter, R. Langtry and S. Volker, "Transition Modelling for General Purpose CFD Codes," Flow Trubulence Combust, 2006.

[47] R. B. Langtry and F. R. Menter, "Correlation-Based Transition Modeling for Unstructured Parallelized Computational Fluid Dynamics Codes," *AIAA Journal,* vol. 47, no. 12, pp. 2894-2906, 2009.

[48] ANSYS, "ANSYS Fluent User's Guide," SAS IP, Inc, 2017.

[49] K. Son, J. Choi, W.-P. Jeon and H. Choi, "Effect of Free-Stream Turbulence on the Flow over a Sphere," American Institute of Physics, 2010.

[50] R. Taghavi-Zenouz, M. Salari, M. M. Tabar and E. Omidi, "Hot-wire Anemometry of Transitional Boundary Layers Exposed to Different Freestream Turbulence Intensities," Department of Mechanical Engineering, Iran University of Science and Technology, Narmak, Tehran, Iran, 2008.

[51] FIFA TV, "2014 FIFA World Cup Brazil Television Audience Report," Kantar Media, 2014.

[52] FIFA, "FIFA Quality Programme for Footballs (outdoor, futsal and beach soccer footballs)," FIFA, 2018.

[53] S. Haake, "Sports Engineering," University of Sheffield, 1999.

[54] A.T. Kearney, "The Sports Market; Major trends and challenges in an industry full of passion," A.T. Kearney, Inc, 2011.

[55] M. Ward, *Single Seam Ball Testing,* Loughborough University, 2016.

[57] D. C. Wilcox, Turbulence Modeling for CFD, 2nd Edition ed., D.C.W. Industries, 2004.

APPENDIX A

Procedure for Estimation of Discretization Error [47]

  <u>Step 1</u> Define a representative cell, mesh or grid size h. For example for three-dimensional calculations

$$h = \left[\frac{1}{N} \sum_{i=1}^{N} (\Delta V_i) \right]^{1/3} .$$
(1)

For two-dimensions,

$$h = \left[\frac{1}{N} \sum_{i=1}^{N} (\Delta A_i) \right]^{1/2}$$
(2)

where ΔV_i is the volume and ΔA_i is the area of the ith cell, and N is the total number of cells used for the computations. Eqs. (1) and (2) are to be used when integral quantities, e.g., drag coefficient is considered. For field variables, the local cell size can be used. Clearly, if an observed global variable is used, it is then appropriate to use also an average "global" cell size.

  <u>Step 2</u> Select three significantly different set of grids, and run simulations to determine the values of key variables important to the objective of the simulation study, for example, a variable ϕ critical to the conclusions being reported. It is desirable that the grid refinement factor, $r=h_{coarse}/h_{fine}$, be greater than 1.3. This value of 1.3 is based on experience, and not on formal derivation. The grid refinement should, however, be done systematically, that is, the refinement itself should be structured even if the grid is unstructured. Use of geometrically similar cells are preferable.

  <u>Step 3</u> Let $h_1 < h_2 < h_3$ and $r_{21}=h_2/h_1$, $r_{32}=h_3/h_2$, and calculate the apparent order, p, of the method using the expression

$$p = \frac{1}{\ln(r_{21})} \left| \ln |\varepsilon_{32}/\varepsilon_{21}| + q(p) \right| ,$$
(3a)

$$q(p) = \ln \left(\frac{r_{21}^p - s}{r_{32}^p - s} \right) ,$$
(3b)

$$s = 1 \cdot \text{sign}(\varepsilon_{32}/\varepsilon_{21}) ,$$
(3c)

where $\varepsilon_{32}=\phi_3-\phi_2$, $\varepsilon_{21}=\phi_2-\phi_1$, ϕ_k denoting the solution on the kth grid. Note that $q(p)=0$ for $r=const$. Eq. (3) can be solved using fixed-point iteration, with the initial guess equal to the first term. The absolute value in Eq. (3a) is necessary to ensure extrapolation towards $h=0$ (Celik & Karatekin [3]). Negative values of $\varepsilon_{32}/\varepsilon_{21}<0$ are an indication of oscillatory convergence. If possible, the percentage occurrence of oscillatory convergence should also be reported agreement of the observed apparent order with the formal order of the scheme used can be taken as a good indication of the grids being in the asymptotic range; the converse should not necessarily be taken as a sign of unsatisfactory calculations. It should be noted that if either $\varepsilon_{32}=\phi_3-\phi_2$ or $\varepsilon_{21}=\phi_2-\phi_1$ is "very close" to zero, the above procedure does not work. This might be an indication of oscillatory convergence or, in rare situations, it may indicate that the "exact" solution has been attained. In such cases, if possible, calculations with additional grid refinement may be performed; if not, the results may be reported as such.

<u>Step 4</u> Calculate the extrapolated values from

$$\phi_{ext}^{21} = (r_{21}^{p}\phi_1 - \phi_2)/(r_{21}^{p} - 1);$$ (4)

Similarly, calculate $\phi_{ext}{}^{32}$.

<u>Step 5</u> Calculate and report the following error estimates, along with the apparent order p:

Approximate relative error:

$$e_a^{21} = \left| \frac{\phi_1 - \phi_2}{\phi_1} \right| ,$$ (5)

Extrapolated relative error:

$$e_{ext}^{21} = \left| \frac{\phi_{ext}^{12} - \phi_1}{\phi_{ext}^{12}} \right| ,$$ (6)

The fine grid convergence index:

$$\text{GCI}_{fine}^{21} = \frac{1.25 e_a^{21}}{r_{21}^{p} - 1} ,$$ (7)

Table 1 illustrates this calculation procedure for three selected grids. The data used is taken from Celik & Karatekin [3]), where the turbulent two-dimensional flow over a backward facing step was simulated on non-uniform structured grids with total number of cells N_1, N_2, and N_3. Hence, according to Table 1, the numerical uncertainty in the fine-grid solution for the reattachment length should be reported as 2.2%; note this does not account for modeling errors.

Table 1: Sample calculations of discretization error

	ϕ = dimensionless reattachment length (*with monotonic convergence*)	ϕ = axial velocity at x/H=8, y=0.0526 (*p < 1*)	ϕ = axial velocity at x/H=8, y=0.0526 (*with oscillatory convergence*)
N_1, N_2, N_3	18000, 8000, 4500	18000, 4500, 980	18000, 4500, 980
r_{21}	1.5	2.0	2.0
r_{32}	1.333	2.143	2.143
ϕ_1	6.063	10.7880	6.0042
ϕ_2	5.972	10.7250	5.9624
ϕ_3	5.863	10.6050	6.0909
p	1.53	0.75	1.51
$\phi_{ext}{}^{21}$	6.1685	10.8801	6.0269
$e_a{}^{21}$	1.5%	0.6%	0.7%
$e_{ext}{}^{21}$	1.7%	0.9%	0.4%
$GCI_{fine}{}^{21}$	2.2%	1.1%	0.5%